# Remanent magnetization, magnetic coupling and interface ionic configurations of intergrown rhombohedral and cubic Fe-Ti oxides: a short survey

Robinson, Peter[1], McEnroe, S.A.[2], Miyajima, Nobuyoshi[3], Fabian, Karl[1] and Church, Nathan[2]

[1]Geological Survey of Norway, N-7491, Trondheim, Norway
[2] Norwegian University of Science and Technology, N-7491 Trondheim, Norway
[3] Bayerisches Geoinstitut, Universität Bayreuth, D-95440, Germany

## Abstract

Some intergrowths between rhombohedral and cubic Fe-Ti oxides show properties of high remanence and stability, greater than can be explained solely by properties of the individual phases. Magnetic experiments demonstrate magnetic coupling across the interfaces between these phases. These have similarities to intergrowths solely of rhombohedral oxides with the properties of lamellar magnetism. Long-known studies indicate the common interface is along (111) octahedral planes of the cubic phase and (001) of the rhombohedral phase. This is confirmed in new TEM results on a synthetic titano-hematite and on a natural ferri-ilmenite, both with reduction-exsolution lamellae of magnetite, where high-resolution lattice-fringe images demonstrate a common orientation of Fe octahedra along the interface. Such information provides a starting point to investigate atomic configurations, ionic charge imbalance, and magnetic moments along these interfaces, and leads toward a new application of the theory of lamellar magnetism. (141 words)

## Introduction

Worldwide studies of igneous and metamorphic rocks and synthetics, some with unusual magnetic properties, provide examples of intergrowths of rhombohedral exsolution lamellae in cubic hosts and vice-versa. All appear related to local 'oxidation' or 'reduction' conditions during genesis, but whether such processes are driven by environmental changes external to individual rocks, or only internal reactions, can only be understood on an individual basis. The classic example is of rhombohedral ilmenite lamellae exsolved from

titanomagnetite by oxidation, resulting in movement of the residual magnetite composition toward the Ti-free end member. A 'parallel', but less well known example, is of cubic magnetite exsolved from ferri-ilmenite by reduction, resulting in movement of the residual ilmenite host composition toward an $Fe^{3+}$-free end member. In these two examples, both intergrowths may occur together in the same rock, suggesting a local exchange of oxygen with no influence of an external source.

Another example of a rhombohedral host is Ti-free hematite with very fine lamellae of magnetite or magnetite-maghemite solid solution. Its origin is uncertain, perhaps produced by high-grade metamorphism of an older hematite ore, itself derived by well known desilication of banded iron formation (Schmidt et al. 2007).

A synthetic example, also with a rhombohedral host, consists of a metastable titanohematite solid solution of Ilm40 composition with reduction exsolutions of magnetite. This was produced by slight reduction during an attempt at synthesis of a single-phase rhombohedral oxide. Other recent experimental work on synthetic ferri-ilmenite in the composition range ilm50-ilm70, with metastable phase separation between ordered and disordered rhombohedral phases, has shown profound effects on the magnetic properties and the mechanism of self-reversal (Nord and Lawson, 1989; Lagroix et al 2004; Fabian 2011; Robinson et al 2012, 2013;).

Several of the samples with rhombohedral-cubic intergrowths provide evidence of unusual magnetic properties, including high natural remanent magnetizations (NRM) and coercivity, possibly enhanced by magnetic coupling between the phases, that must occur along the well established common interface which is (001) in the rhombohedral oxide and (111) in the cubic oxide (Ramdohr 1980). For a natural ilmenite sample from Australia, and for the exsolved Ilm 40 sample, we have high-resolution TEM data providing exact information on the relative orientation of the rhombohedral and cubic phases across the

interface, and a starting point to examine atomic configurations and the possible origin of the magnetic properties.

## Natural and synthetic examples

### Lamellae of ilmenite in magnetite

The first example involves 'oxidation-exsolution' of ilmenite from titanomagnetite. Here a magnetite host contains lamellae of ilmenite on the magnetite (111) planes, which are shared with (001) of ilmenite (Figure 1), and is highlighted in the extensive work of Paul Ramdohr (1980). Ramdohr considered this intergrowth to be a product of true exsolution from a cubic solid with a major ilmenite component. Using a series of experiments under controlled conditions of oxygen fugacity, Lindsley (1962) and Buddington and Lindsley (1964) demonstrated that the intergrowth could be produced from a stoichiometric cubic titanomagnetite by oxidation during falling temperature. This reaction was repeated in more recent experimental studies (Lattard 1995, Lattard et al. 2005, Evans et al. 2006, Sauerzapf et al. 2008). It is illustrated schematically in the ternary phase diagram used by Lindsley (1991) (Figure 2). The diagram has two highly useful properties: 1) The three binary solid solutions Ulvöspinel-Magnetite, Ilmenite-Hematite, and Ferropseudobrookite-Pseudobrookite lie on parallel lines, and 2) Lines of variable oxygen fugacity but constant Ti/Fe ratio are parallel to the base. It is thus very easy to see that an increase in local oxygen fugacity (Figure 2, Reaction A) can cause a Ti-bearing magnetite to evolve to an intergrowth of Ti-poor magnetite plus lamellae of ilmenite.

From a magnetic point of view, the effects of this oxy-exsolution are somewhat ambiguous. If the ilmenite lamellae (paramagnetic at room $T$) are sufficiently thick and abundant, such that the subdivided magnetite is not interacting across the lamellae, then this can result in smaller magnetic domain sizes in the magnetite. This should lead to a stronger and more stable natural remanent magnetization compared to multi-domain magnetite

(Strangway et al. 1968; Larson et al. 1969; Shive and Butler 1969; Evans and Wyman 1974; McEnroe 1996a,b; Harrison and Putnis, 1997; Evans et al. 2006). Harrison et al. (2002) studied such a possible effect in magnetite with thin true exsolution lamellae of ulvöspinel and observed the formation of magnetic "superstates", where interactions across lamellae generate flux closure structures between multiple particles that mimic vortex states and 180-degree domain walls. In such cases the development of exsolution microstructure does not cause a shift from MD to SD bulk magnetic properties despite the reduction in particle size. It is unclear how common such strong interactions and magnetic superstates are in natural samples. It is also possible that magnetostatic coupling might change the bulk properties towards higher coercivity. In magnetite-ilmenite intergrowths the potential magnetic effects along the (111)-(001) magnetite-ilmenite lamellar contacts are also to be considered (see below).

**Lamellae of magnetite in ilmenite**

The second example, ilmenite with magnetite exsolution, is from intrusions with significant remanent magnetic anomalies in South Australia, the Black Hill Norite (Rajagopalan et al. 1993; Schmidt et al. 1993; Foss and McKenzie 2011;) and in West Australia, Mount Harcus (Austin et al. 2014). These intrusions have NRM values significantly higher than the induced magnetization, resulting in remanent-dominated anomalies. Full investigation of the mineralogical carriers of these anomalies is ongoing and only highlights are presented here.

The Black Hill Norite (BHN) has a highly stable NRM of up to 9.5 A/m, and two coercivity components. A low-coercivity component is carried by the oxy-exsolved MD magnetite with minor ilmenite lamellae. The second component, above 100 mT, is very high for magnetite and is responsible for the bulk of the NRM, and the remanent anomaly. Figure 3 shows magnetite grains with (111) oxy-exsolution lamellae of ilmenite, and co-existing

discrete ilmenite with bright lamellae parallel to (001) of the host. These bright lamellae show remarkably straight (001) boundaries and abrupt lamellar edges normal to (001), a shape that is distinct from normal hematite exsolution lamellae in ilmenite. These prove to be magnetite, and their presence can be explained by 'reduction' exsolution of ferrian ilmenite to an intergrowth of near end-member magnetite plus more titanian ilmenite, as shown in Figure 2, Reaction B. TEM images of Black Hill ilmenite with magnetite exsolution provided information on interface and lattice orientations, as discussed below. The oxy-exsolution in the magnetite host and reduction exsolution in the ilmenite host are likely controlled by local exchange of oxygen during cooling within the rock, without either addition or subtraction of oxygen from another source (coupling in Figure 2, Reactions A and B across an intermediate bulk composition).

The example from Mt Harcus, West Australia, has more complex intergrowths. The intrusion has a very high average NRM of 25 A/m (Church 2015). Experiments show that there are two distinct coercivity components from different domain states in the magnetite. Magnetite grains (> 600 μm) contain a few large oxy-exsolution lamellae of ilmenite, ~100 μm thick. These ilmenites contain much finer reduction-exsolution lamellae of magnetite. In both the BHN and Harcus, the finer magnetite lamellae in ilmenite are of pseudo-single-domain size and could contribute to the strong NRM, potentially enhanced by magnetic phenomena along phase interfaces.

**Lamellae of magnetite in hematite**

The third natural example is of coarse-grained metamorphic Ti-free hematite from the Peculiar Knob Deposit, South Australia. An NRM of 120 A/m is required to model the magnetic anomaly generated by the ore bodies (Schmidt et al., 2007) and NRM values above 200 A/m occur in hematite-rich cores. These samples have coercivity and NRM values greater than expected for pure multi-domain hematite. Observations in reflected-light (Figure

4), followed by electron microprobe (EMP) analyses, showed the hematite contains fine

intergrowths of thin layers parallel to (001) with a higher Fe content than pure hematite,

which were concluded to be either magnetite, or magnetite-rich members of the magnetite-

maghemite solid solution series. The high coercivity and stable remanence is considered to

be a combination effect of fine-grained magnetite and of the remanence of contact layers

within a weakly magnetic hematite host.

To evaluate the contributions of the two phases, measurements of magnetic saturation

($M_S$), magnetic remanence ($M_R$) and susceptibility, were made from room-$T$ to 700$^o$C in a

Princeton vibrating sample magnetometer (VSM) with a furnace installed, using the method

of Fabian et al. (2013). Shown in Figure 5 are the interpolated $M_S$ and $M_R$ curves with

temperature. The Ms-$T$ curve and low-field susceptibility both show two components, at

575$^o$C (magnetite) and at 675$^o$C (hematite). Already the unusual shape of the $M_S$ curve below

575$^o$C, with its intermediate peak at 500 $^o$C, likely results from the two exchange coupled

phases. There is also a corresponding peak in low-field susceptibility. In accordance with

theory, the peak in high-field susceptibility, that indicates the magnetite ferromagnetic $T_C$,

occurs at a slightly higher $T$. The antiferromagnetic hematite should not show a high-field

susceptibility peak, but, due to noise, the data in Figure 5 are not conclusive.

The $M_R$ curve is broader, likely indicating a slightly wider $T$ range for magnetite unblocking,

due to coupling at magnetite-hematite interfaces with variable surface/volume ratios. The

Néel $T$ for the hematite is 675$^o$C, in good agreement for a near end-member composition from

EMP data. Low-temperature magnetic data also indicate coupling between the fine magnetite

lamellae and the host hematite. Backwards extrapolation to room $T$ of the hematite Ms at 600

$^o$C, above the magnetite $T_C$, indicates that about 10% (0.03 of 0.33 Am$^2$/kg) of the iron-oxide

Ms at room $T$ originates from magnetite. The room-$T$ Ms of magnetite is ~91 Am$^2$/kg, while

the weak canted moment of hematite has an Ms of ~0.3 Am$^2$/kg. This gives ~330 ppm of

magnetite in hematite. The intermediate $M_S$ peak can be interpreted as an exchange-coupling release of magnetite moments along the hematite-magnetite interfaces. The size of this peak, about the same size as the total magnetite moment, indicates a ratio of coupled surface layer to total volume of ~1:2. Assuming the thickness of the exchange-pinned magnetite surface layer to be one exchange length (~ 9 nm) this implies some magnetite grain sizes are around 35 nm. In this size range magnetite exchange coupled to hematite is single-domain and would carry a very high and stable remanence.

Hematite has a small in-plane anisotropy within (001) and a large out-of-plane anisotropy out of (001). Exchange coupling is strong. If the magnetite is exchange coupled to neighboring hematite layers along the magnetite – hematite interface, then it prevents the spins in the surface magnetite layers from rotating out of the hematite (001) easy direction. Because domain nucleation in small magnetite lamellae is mainly initiated at corners and edges, and to lesser extent around defects, this additional interface anisotropy inhibits nucleation of domain walls and effectively increases the coercive force and, therefore, the capacity for carrying remanent magnetization. Three effects may lead to high remanence in magnetite-hematite intergrowths: 1) Strain induces internal stress fields in magnetite, that add to the magnetocrystalline anisotropy and transform magnetite into a magnetically harder material (Hubert and Schäfer, 1998). Strain due to inclusions in hematite is proposed to enhance coercivity by magnetoelastic pinning of moments in the lattice (Özdemir and Dunlop 2006). 2) Additional lamellar magnetic moments increase the "effective $M_S$". In magnetite, due to its large ferrimagnetic bulk moment, however, this should be a noticeable effect only for very tiny lamellae. 3) Exchange coupling across the magnetite-hematite interface adds a possibly large surface anisotropy to the bulk-magnetic anisotropy of magnetite. Spins at the magnetite surface, by this coupling, may experience additional magnetocrystalline

anisotropy from the hematite. Reduced movability of spins hinders nucleation of domain walls and thus increases the remanence capacity.

The Peculiar Knob deposit appears to have originated as Early Proterozoic banded iron formation that underwent silica leaching, to produce a massive hematite deposit, later subjected to high-grade regional metamorphism. The magnetite was either a relict component from the original iron formation or magnetite was being produced by partial reduction of hematite (Figure 2, Reaction C) during the culminating high-grade metamorphic event. Such a reduction, with a resulting similar oriented intergrowth was produced experimentally by Keeling and Wick (1963).

**Lamellae of magnetite in synthetic titanohematite**

Our final example is a synthetic sample of titanohematite, nominally Ilm 40, a composition that should be chemically disordered almost completely and antiferromagnetic (Fabian et al 2015). Magnetic experiments demonstrate that it contains a component close to pure magnetite in addition to the host Ilm 40. The plot of $M_S$-T (Figure 6) shows a significant loss in saturation magnetization near 345$^{\circ}$C, the $T_N$ of Ilm40. The amount of magnetization lost (~0.2 Am$^2$/kg) in relation to the theoretical ferrimagnetic saturation magnetization (~58 Am$^2$/kg) indicates a small degree of remaining chemical order (Q~0.004) that produces a small ferrimagnetic component in Ilm 40. Above 345$^{\circ}$C, 42% of the saturation magnetization remains with a steady loss until reaching the 535$^{\circ}$C $T_C$ of the magnetite nanoparticles, or bulk magnetite (X < 0.07, using a curve calculated by Bleil and Petersen, 1981), with a small amount remaining to 545$^{\circ}$C. Extrapolating this magnetite magnetization backwards to room $T$ and comparing it to the magnetite bulk $M_S$ of about 91 Am$^2$/kg yields an estimated magnetite concentration of about 0.2 %. The $M_R$ curve shows a significantly different behavior, in that above the $T_N$ of Ilm40 no measurable remanence remains. Both the high-field and low-field

9

susceptibility measurements indicate a $T_C$ of 535$^o$C for the magnetite lamellae, and the low-field susceptibility for the Ilm 40 has a distinct drop at 345$^o$C, the $T_N$ of Ilm40.

The difference between the $M_S$ and $M_R$ curves is due to the changing behavior of the thin magnetite lamellae with temperature. The lamellae are superparamagnetic above the $T_N$ of Ilm$_{40}$, and therefore hold no remanence, but they do have an induced magnetization in the 1.5 T field up to $T_C$, as shown in the $M_S$ curve. Below the $T_N$ of the Ilm40 the nanoscale magnetite lamellae are exchange coupled to the disordered titanohematite host, which stabilizes their magnetization. This results in a measurable remanence in both the disordered titanohematite host, itself nominally antiferromagnetic, and the ferrimagnetic magnetite lamellae. Above the $T_N$ of Ilm$_{40}$, where the exchange coupling is broken, the magnetite lamellae become superparamagnetic and cannot carry a remanence. Because the paramagnetic lm40 dominates the magnetic susceptibility between 360 $^o$C and 520$^o$C it was not possible to fit Langevin curves to the available data in order determine magnetite grain sizes by another independent method.

Although magnetite was detected magnetically, its presence was not found using X-ray powder diffraction, that yielded a pattern with no line broadening, and refined parameters $a = 5.0557$Å, $c = 13.8528$Å, and V $= 306.646$Å$^3$, yielding an inferred composition Ilm 40.5 from a standard working curve. Magnetite was found with difficulty using TEM (Figure 7). Based on magnetic data, it is present in an amount < 0.2%. TEM images demonstrate that the magnetite occurs in lamellae ~4.5-5.8 nm thick (~3-4 unit cells) parallel to (001) of the titanohematite, and provided key information on the exact positioning of the rhombohedral and cubic lattices discussed below. The Curie temperature for magnetite nanoparticles depends on size and shape. Computations (Shcherbakov et al., 2012) and experimental data (e.g. Sadeh, 2000) indicate that for particles with sizes of 5-10 nm $T_C$ can easily lie 50 K lower than for bulk material in stoichiometric magnetite, which fits to the observed low $T_C$

10

value.  The slight magnetite exsolution from the titanohematite likely resulted from very

slight reduction of the titanohematite during synthesis, producing magnetite plus a very

slightly more Ti-rich ilmenite (Figure 2, Reaction D).

### Orientation of cation-oxygen octahedra on the rhombohedral-cubic interface

There is little doubt that the phase interface must involve common octahedral layers in

the two phases, normally 2/3 occupied and 1/3 vacant in the rhombohedral phase, but 3/4

occupied and 1/4 vacant in the cubic phase, except for maghemite with octahedral vacancies

of unknown location. An average occupancy between 2/3 and 3/4 is 0.7083.

The TEM images and accompanying lattice-fringe images of Figure 7B and Figure 8

provide special opportunities to obtain information about phase orientations across the

rhombohedral-cubic interface.  The zone axis orientation of the lattice image in Figure 7B is

such that $001^*_h$ (of hexagonal hematite) is parallel to $111^*_c$ (of cubic magnetite). In standard

terminology for reciprocal lattices, 001* is a vector normal to (001) whereas 111* is a vector

normal to (111).   This confirms that the mutual phase interface is (001) of hematite and (111)

of magnetite. The zone axis orientation of the lattice-fringe image is also such that $\boldsymbol{a}^*_h$ (of

hexagonal hematite) is exactly parallel to -2 0 2$^*_c$ (of cubic magnetite).  Here $\boldsymbol{a}^*_h$ in the

hexagonal system refers to a vector normal to a hematite $\boldsymbol{a}$ axis and -202$^*_c$ in the cubic system

refers to a vector normal to a (-202) plane.  These observations provide the essential first key

to atomic arrangements on the common interface.

Related information is provided in Figure 8.  Figure 8A provides separate lattice-

fringe images, in common orientation, on opposite sides of a magnetite-ilmenite interface

shown in low resolution.  It is easy to see that $\boldsymbol{c}^*$ ilmenite is parallel to 111* of magnetite, and

that $\boldsymbol{a}_1^*$ of ilmenite is parallel to 2 0 -2* of magnetite (symmetrically equivalent to -2 0 2* in

Figure 7B). Figure 8B is a high-resolution image of the sample, in the same orientation, in

which alternate octahedral and tetrahedral-octahedral layers in magnetite parallel to the

interface are directly imaged.  As is common with such edge-on images, details of the

interface itself are not resolved, though it is confined to a thickness of about 1 nm equivalent

to 4 atomic layers.  The selected area electron diffraction pattern (SAED in inset) in the

lattice-fringe image shows diffraction spots for both phases.  An interesting feature of Figure

8A is the prominent 003 diffraction spot (first spot from the origin along $c^*$) that is

characteristic of Fe-Ti ordered ilmenite and the absence of this spot in the SAED pattern in

Figure 7B which is of an Fe-Ti disordered titanohematite.

Figure 9 provides an explanation for how a zone axis as in Figure 7B (and Figure 8)

can lie exactly along a line that is in the same position perpendicular to $001^*_h$ and $111^*_c$, and

also perpendicular to $a^*_h$ and   $-2\ 0\ 2^*_c$, and where $a^*_h$ and $-2\ 0\ 2^*_c$, both also lie exactly in

the interface plane and both on the edge of an octahedron internal to the cubic unit cell.

Based on the known orientation of cation-oxygen octahedra with respect to the $a$ axes of

hematite (Figure 10), one can then portray the octahedral orientation on the common cation

plane, though only schematically and without reference to actual octahedral occupancies or

distortions.  When the octahedral layers of the two structures are superimposed one can

identify individual rings of six yellow-colored octahedra (yellow flower) around a vacancy

that are in fact octahedra that can be in common for both hematite and for magnetite,

providing only 0.50 (6/12) of possible occupancy.

Details of occupancy, outside the central common array, are a complex issue, dealt

with in Figure 11 and Table 1.  For ease of discussion, both the rhombohedral and cubic

structures are portrayed in arrays of undistorted uniform octahedra and tetrahedra, though the

distortions, especially in hematite, are considerable, as discussed later. The dashed black lines

mark the boundaries of a 'super cell' created by selecting equivalent points at the centers of

the 'yellow flowers' that are atomic vacancies common to both structures. This is four times

the standard footprint of a rhombohedral unit cell containing 2 octahedrons (outlined by the

pattern of vacancies in Figure 11A), and is three times the standard footprint of a constructed

hexagonal cell of a cubic oxide (outlined by the pattern of vacancies in Figure 11B). Within

the supercell, each octahedral layer (Figure 11A,B) contains 6 yellow octahedra, exactly half

the total maximum of 12. Within each tetrahedral-octahedral layer of cubic oxide (Figure

11C,D) there are 3 octahedra (violet), 3 up-pointing tetrahedra (red), and 3 downward-

pointing (orange). Within the supercell there are 12 oyxgens at each level.

Figure 11A shows a standard dioctahedral array as in hematite. To bring the total to a

hematite-like occupancy (0.6667) beyond the central yellow flower is equivalent to adding

two more filled octahedra (8/12), indicated in green in Figure 11A. Such an addition is no

problem in the rhombohedral oxide itself, but difficult when this layer is juxtaposed against a

tetrahedral-octahedral layer of a cubic oxide. To bring the total to a magnetite-like occupancy

(0.75) would be equivalent to adding three more filled octahedra (9/12). These are indicated

in green for magnetite in Figure 11B in positions that are perfect with respect to an adjacent

tetrahedral-octahedral layer. Both additions to the supercells preserve trigonal symmetry of

the octahedral layers. Our initial thoughts, based on rhombohedral oxides, were that common

'contact layers' between the two structures should have an average between 8 and 9 filled

octahedra. However, charge-balance considerations for the interfaces studied here, invalidate

that concept.

### Occupancy of cation-oxygen octahedra and tetrahedra

### near the rhombohedral-cubic interface

The first step to understanding the arrangements between rhombohedral and cubic

layers at an interface is to understand first how it works perfectly in a cubic oxide. For this,

consider how the tetrahedral-octahedral layer of Figure 11D fits over the magnetite octahedral

layer of Figure 11B. The triangular pits in the upper surface of the octahedral layer can be

thought of as small 'sugar bowls'. Each bowl has a lid composed of one of the violet

13

octahedrons, which shares three edges with the rim of the bowl. Then notice the places where three octahedral apices meet at a single point on the top of the octahedral layer.  To these are attached the downward pointing apices of the orange tetrahedrons. Finally, notice the empty locations in the octahedral layer.  The upward pointing red tetrahedrons fit exactly over these openings, thus sharing three apices with oxygens around the upper edge of the opening. This entire fit, just described, is a shown in transparent form in Figure 11F.

Each oxygen in the magnetite structure is coordinated by 3 Fe octahedra and 1 Fe tetrahedron.  An interesting phenomenon, well known in magnetite above the Verwey transition, is that the charge of the octahedral ions (as distinct from tetrahedral) is not 'localized', i.e. one cannot predict whether a given ion is $Fe^{2+}$ or $Fe^{3+}$.  For charge-balance considerations an average charge of 2.5+ is used.  Thus, the contributions to one oxygen are 3 x 2.5/6 = 1.25 and 1 x 3/4 = 0.75, total = 2.  The perfect charge balance in magnetite is summarized in Table 1, Part1.

Attempts to fit magnetite tetrahedral-octahedral layers to rhombohedral octahedral layers run into a different class of problems, that can be understood by placing the tetrahedral-octahedral layer of Figure 11D over the rhombohedral octahedral layer of Figure 11A, shown in transparent form in Figure 11E.  There are no triangular pits, but the violet octahedrons do share edges with two instead of three octahedrons.  There are no triple junctions between octahedrons, so the orange tetrahedrons link their lower apices only to two octahedrons below. There are four openings at the corners of the octahedral layer supercell, over which one places upward-pointing red tetrahedrons, but two of these tetrahedrons must share faces with green octahedrons, a strong contrast with magnetite, where the openings are perfectly placed. Could the green octahedrons be placed differently, like some of those in Figure 11B? Probably not, because such occupancy would place three octahedrons in a row along $c$ with

two shared faces between the three. Therefore, the present outlook favors limited tetrahedral face sharing.

The concept to have an average occupancy between 2/3 and 3/4 occupancy in the octahedral layer is abandoned when realizing that 3+ ions in 8 octahedral sites actually provide more positive charge than 2.5+ ions in 9 octahedral sites. Increased positive charge is needed when matching an octahedral layer to a tetrahedral-octahedral layer and that further to a magnetite octahedral layer.

Table 1, Part 2 shows one set of compromises used to minimize what is necessarily charge imbalance at the phase interface between hematite and magnetite, though proof presently is lacking if these specific compromises exist. The simple approach used here may prove illusory, where assignment of charge to ions in different sites in oxides has proved challenging (Coey 2004), more so when dealing with interfaces between two oxides.

Table 1 is arranged in series of pairs of cation layers within the supercell from top to bottom, each pair with 12 coordinating oxygens above, 24 in the middle, and 12 below. Table 1, Part 1 uses this method to demonstrate perfect charge balance in magnetite. The number of pairs of layers both above and below a phase interface is determined by the need to arrive at charge balance, where imbalance is an inherent feature of the interface. The top hematite layer at a hematite-magnetite interface, as indicated in Table 1, Part 2, remains, as in pure hematite, with 8 octahedrons each with $Fe^{3+}$ ions. The tetrahedral-octahedral layer is partly unusual for end-member magnetite: 3 octahedra with $Fe^{2.5+}$ (usual), 4 tetrahedra with $Fe^{3+}$ (usual), and 2 tetrahedra with only $Fe^{2.5+}$ (a lower charge also found in ulvöspinel and hercynite). Bosi et al. (2009) suggest there is easy substitution of $Fe^{2+}$ in tetrahedral sites in magnetite-ulvöspinel solid solutions.

It is speculated that these are the tetrahedra sharing faces with octahedra. In this unusual arrangement around one oxygen, there would be two $Fe^{3+}$ octahedra, providing 2 x

$3/6 = 1$, 1 $Fe^{2.5+}$ octahedron providing 1 x 2.5/6 = 0.4166, and one $Fe^{2.5+}$ tetrahedron providing 1 x 2.5/4 = 0.625, total 2.0417. For this group of layers, the positive charge is 48.5 versus -48 for oxygen, a slight overcharge (+0.5% per oxygen). In the underlying pair of layers, including the tetrahedral-octahedral layer just described, and a normal magnetite octahedral layer, the positive charge is 47 versus -48 for oxygen, a slight undercharge (-1% per oxygen), and altogether as close to balance as one might expect.

The challenge for an interface involving ilmenite is more severe, most particularly because a normal ilmenite Fe octahedral layer is occupied only by $Fe^{2+}$. The charge model adopted for this is given in Table 1, Part 3. The top ilmenite Fe contact layer cannot be against a tetrahedral-octahedral layer without an increased charge, in this case 3 octahedrons with unusual $Fe^{3+}$ ions, and 5 octahedrons with usual $Fe^{2+}$ ions. In combination with the overlying ilmenite Ti layer this creates a positive charge of 51 versus -48 for oxygen, an overcharge (+3% per oxygen). Charge deficiency cannot be made up by adding Ti to the magnetite, because such an addition to the tetrahedral-octahedral layer, actually decreases the charge. Thus, the tetrahedral-octahedral layer below the contact layer is completely usual: 3 octahedra with $Fe^{2.5+}$, and 4 tetrahedra with $Fe^{3+}$. In this pair of layers, the contact layer and the tetrahedral-octahedral layer just described, the positive charge is 44.5 versus -48 for oxygen, an undercharge (-3.6% per oxygen), rather less satisfactory than the interface involving a hematite host. To keep these charge imbalances in perspective, Table 1, Part 4 shows the charge imbalances involving contact layers along an (001) interface between ilmenite and hematite. There the imbalances are larger (+4% and -4%) than those calculated for the rhombohedral-cubic interfaces suggested here.

**Detailed cation positions and nature of strain on the rhombohedral-cubic interface**

This task has required re-examination of the rhombohedral and cubic structures, with a few surprises. The hematite structure of Blake et al. (1966) has features that are well

16

portrayed in the original work but rarely emphasized (Figure 12).  The fact that shared faces of octahedra and non-shared faces of octahedra have different dimensions, yet occur in the same plane, requires that the structure of each oxygen plane have distortions, and that alternate layers are distorted oppositely.  The result is that the trigonal axes of adjacent layers are out of line by about 5 degrees. This might be related subtly to the spin-canted remanent magnetization of hematite, where sublattice magnetizations in adjacent octahedral layers are misaligned by about $0.13^{o}$ (Robinson et al. 2006b). These distortions show that the type of geometric analysis used in Figure 11 is a considerable simplification.

The detailed structure of magnetite (Fleet 1984) also has distortions (Figure 13), though more subtle.  All the octahedra in the 3/4 octahedral layers are slightly distorted, whereas the octahedra in the tetrahedral-octahedral layers are perfectly symmetrical. The distortions in magnetite are so small that they do not detract from the type of geometric analysis used in Figure 11.

Aside from the distortions between the two structures, it is important to notice that the hexagonal footprint of a cubic cell on the (111) interface has a different size and orientation with respect to the octahedrons than the footprints of hematite and ilmenite on their (001) interface (Figure 14A, B).  This complication has no effect in comparing dimensions normal to the interface. The magnetite parameters '$a$' = 5.9369Å must be reworked into the hematite format '$a$' = 4.5702Å with no difference in '$c$', where magnetite layers have a repeat distance of 14.5424Å. Comparing with ilmenite $a$ = 5.0885 and $c$ = 14.0924, indicates Mag/Ilm strains of 0.8981 along '$a$' and 1.0319 along '$c$'. Hematite, with $a$ = 5.034 and $c$ = 13.750 is smaller than ilmenite in both directions, leading to smaller strain 0.9079 along '$a$' and larger strain 1.0576 along '$c$'.  These strains with cubic oxides completely outclass strains between the rhombohedral oxides where Hem/Ilm for $a$ = 0.9893 and Hem/Ilm for $c$ = 0.9762.

The stretching of magnetite along '*a*' would have a large effect in limiting lateral growth. The compression of magnetite along '*c*' could also limit growth in that direction. The combined effect of stretching along '*a*' and compression along '*c*' would change Fe-O-Fe bond angles, and hence change have some effect on magnetic interactions. This aspect is a valid avenue for future studies.

To provide a more qualitative view of interface strain, an octahedral layer of magnetite and an octahedral layer of hematite (with ilmenite cell dimensions) have been superimposed directly (Figure 14C,D), and the centers of equivalent oxygen atoms in a single layer marked individually after centering the two structures on the common center of a hexagonal ring (yellow flower of Figures 10, 11). Obviously the strain changes from small to large over a very small distance along the common plane, which would create a stretch in magnetite, and a compression on the rhombohedral oxide that would only increase with extended lamellae growth in this direction. Magnetostriction in such regions would likely influence bulk magnetic properties.

Effects of interface strain on magnetic properties of lamellae in titanomagnetite and ferri-ilmenite were studied by Shive and Butler (1969). They concluded that interface strain beyond about 5% would be relieved by periodic lattice dislocations, spaced at ~1.42 nm between magnetite and exsolved ilmenite, and at ~5.85 nm between ilmenite and exsolved hematite. Residual lattice strain would be concentrated near phase interfaces and particularly near dislocations, and hence bulk strain would be greater in thin than in thick lamellae. They calculated that such strain for thin hematite-lamellae in ilmenite would produce higher coercivity than for thick lamellae. Unfortunately, it is unusual to find natural samples with only a single size range of lamellae to confirm this experimentally, though it agrees in general with lamellar magnetism theory. They suggested that magnetic effects of strain in magnetite

with ilmenite lamellae are minimal, and that reduction of domain sizes in magnetite may be
the most important magnetic effect.

Another feature that likely influences morphology of magnetite lamellae in ilmenite
(Figure 3), as contrasted to hematite lamellae in ilmenite, is that interface accommodations
established on a single atomic plane are not repeated again in similar arrangement until
lamellar growth has extended to a thickness of six octahedral layers, or a multiple of six.  A
six-layer repetition of layers A-F, that is well understood along *c* of ilmenite-hematite, turns
out to be also a key feature along a normal to (111) of magnetite. This is illustrated in the left
columns of Figures 15 and 16, where only the layers labeled C are compatible for both the
rhombohedral and cubic phases enclosed in a single rhombohedral host. This last limitation is
in contrast to ilmenite lamellae in hematite where similarity between the two structures is so
close that there is a much freer choice in details of edge interfaces.

## Magnetic role of 'contact layers'

The above discussion makes it clear that the octahedral layers at contacts of the
rhombohedral and cubic layers have a different chemical composition than other layers, and
may well behave as 'contact layers' in a way similar to contact layers in exsolved
rhombohedral oxides (Robinson 2002, 2004).  For such an analysis to work, both the
magnetite and the hematite (or ilmenite) are considered as a series of layers.  In the
rhombohedral oxides we know that the magnetic moments are parallel or at a low angle to the
(001) basal plane.  What about magnetite?  Compared to rhombohedral oxides, the
magnetocrystalline anisotropy of magnetite is weak. Above the Verwey transition at -120$^{o}$C,
the 'magnetically easy' direction is normal to the planes (111), not directly along them.
However, this direction normal to one (111) would actually lie only about 17$^{o}$ from other
(111) planes. The shape anisotropy of susceptibility of magnetite would also favor strong
magnetization parallel to the phase interface. These features, coupled with the stronger

19

anisotropy to be expected from the adjacent rhombohedral oxide, may allow one to consider magnetite magnetization in a layered form. This has been done in Figures 15 and 16.

The magnetic models of Figures 15 and 16 are constructed in a parallel manner to those developed for rhombohedral oxides, with more attention to minimizing charge imbalance, rather than composition averaging. This has involved adjustments to ion occupancies adjacent to interfaces in tetrahedral-octahedral layers as shown in Table 1, Part 2 and in octahedral contact layers in Table 1, Part 3. For the rhombohedral oxide, distinct $Fe^{2+}$ and $Fe^{3+}$ ions are used with the parallel values of 4 and 5µB. For the cubic oxide, the valence of Fe is assigned a charge of 2.5 and hence a magnetic moment of 4.5 µB for octahedral positions, and both 3+ and 2.5+ (unusual) for tetrahedral positions. For the rhombohedral oxide, magnetic moments (where present) alternate between layers. For the cubic oxide, magnetic moments of tetrahedral and octahedral ions are oppositely coupled. In practice, this means that if octahedral layers have positive moments, then tetrahedral-octahedral layers will have net negative moments with a smaller value, combining positive moments of octahedral sites and negative moments of tetrahedral sites. In the models, antiferromagnetic coupling is expected between all layers.

In Figure 15, the host is hematite and the lamella is magnetite. Here the lamellar component involves five different layers peculiar to the contact region. These include the positive moments of two contact layers minus the negative moment of one unbalanced hematite layer, and also minus the negative moments of two tetrahedral-octahedral contact layers. The net lamellar moment for one lamella is only 9µB compared to 64.5µB for three unbalanced layers of magnetite. The magnetite moment would be increased by adding groups of six layers between the magnetite layers, each set of six providing an additional 72µB to the positive net moment.

In Figure 16, the host is paramagnetic ilmenite and the lamella is magnetite. Here the lamellar component involves the positive moments of two contact layers minus the unbalanced negative moment of one conventional tetrahedral-octahedral layer. The net lamellar moment for one lamella is $+53.5\mu B$ compared to a ferrimagnetic moment of $+48\mu B$ for four layers of magnetite. The large increase in the lamellar moment is a direct consequence of the fact that the ilmenite Ti layer is paramagnetic, hence there is no subtraction of a net moment, as in the case of a hematite host. The magnetite moment would be increased by adding groups of six layers between the magnetite layers, each set of six providing an additional $+72\mu B$ to the positive net moment.

Figures 15 and 16 are only initial explorations of the concept that lamellar magnetism may occur even where one of the phases is a cubic oxide.

## Implications

Interfaces of exsolution lamellae of ilmenite in hematite, or hematite in ilmenite have been identified as the source of intense remanent magnetism in oxide intergrowths of phases normally considered to be only weakly magnetic (McEnroe et al. 2001a, 2001b, 2002, 2007a, 2007b; Robinson et al., 2002, 2004, 2006a, 2006b, 2012). Exsolution microstructures in cubic Fe-Ti oxides have also been tentatively linked to magnetic domain size reduction, leading to stronger NRM's. Recently examples have been found where exsolution interfaces between cubic and rhombohedral oxides may also be direct sources of strong and stable remanent magnetization. Investigation of this particular style of remanent magnetization has barely begun and may be a significant explanation for many remanent magnetic anomalies on Earth and other planetary bodies.

## Acknowledgements

21

## References

Austin, J., Hillan, D., Schmidt, P.W., and Foss, C. (2014) Magnetism in the Giles Complex. Preview 2014, 171, 41 – 44. Doi:10.1071/PVv2014n171p41

Blake, R.L., Hessevick, R.E., Zoltai, T. and Finger L.W. (1966) Refinement of the hematite structure. American Mineralogist, 51, 123-129.

Bosi, F., Hålenius, U., and Skogby, H. (2009) Crystal chemistry of the magnetite-ulvöspinel series. American Mineralogist 94, p. 181-189,

Buddington, A.F. and Lindsley, D.H. (1964) Iron-titanium oxides and synthetic equivalents. Journal of Petrology 5, 310-357.

Burton, B.P. (1982) Thermodynamic analysis of the systems $CaCO_3$-$MgCO_3$, $aFe_2O_3$ and $Fe_2O_3$-$FeTiO_3$. Ph. D. Dissertation, State University of New York at Stony Brook.

Church, N., Austin, J., Schmidt, P.W., McEnroe, S.A. (2015) Rock magnetic properties and mineral microstructure in high-remanence samples from ultramafic intrusions. 26th IUGG General Assembly, 22.06-07.09.15, Prague, Czech Republic

Coey, M. (2004) Charge-ordering in oxides. Nature 430, 155-156.

Evans, B. W., Scaillet, B. and Kuehner, S. M. (2006) Experimental determination of coexisting iron–titanium oxides in the systems FeTiAlO, FeTiAlMgO, FeTiAlMnO, and FeTiAlMgMnO at 800 and 900C, 1–4 kbar, and relatively high oxygen fugacity, Contributions to Mineralogy and Petrology 152, 149–167.

Evans, M.E., and Wayman, M. (1974) Investigation of role of ultrafine titanomagnetite intergrowths in paleomagnetism. Geophysical Journal of The Royal Astronomical Society, 36, 1–10.

Evans, M. E., Krása, D., Williams, W. and Winklhofer, M. (2006) Magnetostatic interactions in a natural magnetite-ulvospinel system. Journal of Geophysical Research, 111, doi:10.1029/2006JB004454.

Fabian, K., McEnroe, S.A., Robinson, P. and Shcherbakov, V.P. (2008) Exchange bias identifies lamellar magnetism as the origin of the natural remanent magnetization in ilmeno-hematite from Modum, Norway. Earth Planet. Science Letters, doi:10.1016/j.epsl.2008.01.034.

Faban, K., Shcherbakov, V.P. and McEnroe, S.A. (2013) Measuring the Curie temperature, Geochemistry Geophysics and Geosystems, 14, 947–961, doi:10.1029/2012GC004440.

Fabian, K., Shcherbakov, V.P., McEnroe, S.A., Robinson, P. and B.P. Burton (2015) Magnetic mean-field modeling of solid solutions: Theoretical foundations and application to the hematite-ilmenite system. Geophysical Journal International, doi: 10.1093/gji/ggv199.

Fabian, K., Miyajima, N., Peter Robinson, McEnroe, S.A., Boffa Ballaran, T. and Burton, B. P. (2011) Chemical and magnetic properties of rapidly cooled metastable ferri-ilmenite solid solutions: I. Fe-Ti order transition in quenched synthetic Ilm 61, Geophysical Journal International, 186,997-1014.

Fleet, M.E. (1984) The structure of magnetite: two annealed natural magnetites Fe3.005O4 and Fe2.96Mg0.04O4. Acta Crystallographica C40, 1491-1493.

Foss, C. and McKenzie, B. (2011) Inversion of anomalies due to remanent magnetisation: an example from the Black Hill Norite of South Australia, Australian Journal of Earth Sciences: An International Geoscience Journal of the Geological Society of Australia, 58:4, 391-405, DOI: 10.1080/08120099.2011.581310.

Frandsen, C., Mørup, S., McEnroe, S.A., Robinson, P. and Langenhorst, F. (2007) Magnetic phases in hemo-ilmenite: Insight from low-velocity and high-field Mossbauer spectroscopy, Geophysical Research Letters doi:10.1029/2006GL029063.

Harrison, R.J. and Putnis, A. (1997) The interaction between exsolution microstructures and magnetic properties of the magnetite-spinel solid solution. American Mineralogist 82, 131-142.

Harrison, R.J., Dunin-Borkowski, R.E., and Putnis, A. (2002) Direct imaging of nanoscale magnetic interactions in minerals. Proceedings of the National Academy of Sciences, 99, 16556-16561.

Harrison, R.J., McEnroe, S.A., Robinson, P. and Howard C. (2010) Spin orientation in a natural Ti-bearing hematite: Evidence for an out-of plane component. American Mineralogist, 95, 974–979.

Hubert, A. and Schäfer, R. (1998) The Analysis of Magnetic Microstructures, Springer XXIII, 696 p.

Keeling, R.O., Jr., and Wick, D.A. (1963) Magnetite: Preferred orientation on the basal plane of partially reduced hematite. Science 141, 1175-1176.

Lagroix, F., Banerjee, S. K. and Moskowitz, B. M. (2004) Revisiting the mechanism of reversed thermoremanent magnetization based on observations from synthetic ferrian ilmenite ($y = 0.7$), Journal of Geophysical Research. DOI: 10.1029/2004JB003076

Larson, E., Ozima, M., Nagata, T. and Strangway, D. (1969) Stability of remanent magnetization of igneous rocks. Geophysical Journal of the Royal Astronomical Society, 17, 263-292.

Lattard, D. (1995). Experimental evidence for the exsolution of ilmenite from titaniferous spinel. American Mineralogist 80, 968-981.

Lattard, D., Sauerzapf, U. and Kasemann, M. (2005). New calibration data for the Fe-Ti oxide thermo-oxybarometers from experiments in the Fe-Ti-O system at 1bar, 1000-13008C and a large range of oxygen fugacities. Contributions to Mineralogy and Petrology 149, 735-754.

Lindsley, D.H. (1962) Investigations in the system FeO-Fe2O3-TiO2. Carnegie Institution of Washington Yearbook 61, 100-106.

Lindsley, D.H. (1991) Experimental studies of oxide minerals. Reviews in Mineralogy, 25, 69-106

McEnroe, S.A. (1996a) North America during the Lower Cretaceous: New paleomagnetic constraints from intrusions in New England. Geophysical Journal International, 126, 477-494.

McEnroe, S.A. (1996b) A Barremian - Aptian (Early Cretaceous) paleomagnetic reference pole for North America. Journal of Geophysical Research, 101, 15,819-15,835.

McEnroe, S.A., Robinson, P., and Panish, P.T. (2001a) Aeromagnetic anomalies, magnetic petrology and characterization of ilmenite-and magnetic-rich cumulates of the Sokndal region, Rogaland, Norway. American Mineralogist 86, 1447-1468.

McEnroe, S.A, Harrison, R.J., Robinson, P., Golla, U. and Jercinovic, M.J. (2001b) Effect of fine-scale microstructures in titanohematite on the acquisition and stability of natural remanent magnetization in granulite-facies metamorphic rocks southwest Sweden: Implications for crustal magnetism. Journal of Geophysical Research 106, 30,523-30,546.

McEnroe, S.A., Harrison, R.J., Robinson, P. and Langenhorst, F. (2002) Nano-scale haematite-ilmenite lamellae in massive ilmenite rock: an example of "lamellar magnetism" with implications for planetary magnetic anomalies. Geophysical Journal International, 151, 890-912.

McEnroe, S.A., Harrison, R.J., Robinson, P. Langenhorst, F., Kasama, T., Putnis, A., Jackson, M., Hirt, A. M. and Brown, L. L. (2004) Lamellar magnetism: effects of interface versus exchange interactions in the ilmenite-hematite system. International Conference

on Fine Particle Magnetism, London Center for Nanotechnology, Conference Guide, p. 4-5, UCL, London.

McEnroe, S.A., Carter-Stiglitz, B., Harrison, R.J., Robinson, P., Fabian, K. and McCammon, C. (2007a) Magnetic exchange bias of more than 1 Tesla in a natural mineral intergrowth. Nature Nanotechnology, doi:10.1038/nnano.2007.292.

McEnroe, S.A., Robinson, P., Langenhorst, F., Frandsen C., Terry, M.P., and Boffa Ballaran, T. (2007b) Magnetization of exsolution intergrowths of hematite and ilmenite: Mineral chemistry, phase relations, and magnetic properties of hemo-ilmenite ores with micron- to nanometer-scale lamellae from Allard Lake, Quebec. Journal of Geophysical Research, 112, B10103, doi:10.1029/2007JB004973.

McEnroe. S.A., Fabian, K., Robinson, P., Gaina, C. and Brown, L.L. (2009) Crustal magnetism, lamellar magnetism and rocks that remember. Elements 5, 241-246.

McCammon, C., McEnroe, S.A., Robinson, P. and Burton, B.P. (2009) Mössbauer spectroscopy used to quantify natural lamellar remanent magnetization in single-grains of ilmeno-hematite. Earth and Planetary Science Letters, 288, 268-278.

Nord, G. L. and Lawson, C. (1989) Order-disorder transition-induced twin domains and magnetic properties in ilmenite-hematite, American Mineralogist, 74, 160-176, 1989.

Özdemir, Ö, and Dunlop, D.J. (2006) Magnetic memory and coupling between spin-canted and defect magnetism in hematite, Journal of Geophysical Research, vol. 111, B12S03, doi:10.1029/2006jb004555.

Rajagopalan, S., Schmidt, P.W. and Clark, D.A. (1993) Rock magnetism and geophysical interpretation of the Black Hill Norite, South Australia. Exploration Geophysics 24, 209–212.

Ramdohr, P. (1980) The ore minerals and their intergrowths. International Series in Earth Science, 35, 1207 p. Pergamon Press, Frankfurt.

Robinson, P., Harrison, R.J., McEnroe, S.A., and Hargraves, R.B. (2002) Lamellar magnetism in the hematite-ilmenite series as an explanation for strong remanent magnetization. Nature, 418, 517-520.

Robinson, P., Harrison, R. J., McEnroe, S.A. and Hargraves, R.B. (2004) Nature and origin of lamellar magnetism in the hematite-ilmenite series, American Mineralogist, 725-747.

Robinson, P., Harrison, R. J. and McEnroe, S. A. (2006a) $Fe^{2+}$ / $Fe^{3+}$ charge ordering in contact layers of lamellar magnetism: Bond valence arguments. American Mineralogist 91, 67-72.

Robinson, P., Heidelbach, F., Hirt, A.M., McEnroe, S.A. and Brown, L.L. (2006b) Crystallographic-magnetic correlations in single crystal hemo-ilmenite: New evidence for lamellar magnetism. Geophysical Journal International 165, 17-31.

Robinson, P., Fabian, K., McEnroe, S.A. and Heidelbach, F. (2013) Influence of lattice-preferred orientation with respect to magnetizing field on intensity of remanent magnetization in polycrystalline hemo-ilmenite. Geophysical Journal International. doi: 10.1111/j.1365-246X.2012.05692.x

Robinson, P., Harrison, R. J., Fabian, K. and McEnroe, S. A. (2012) Chemical and magnetic properties of rapidly cooled metastable ferri-ilmenite solid solutions: implications for magnetic self-reversal and exchange bias, III. Magnetic interactions in samples produced by Fe-Ti ordering, Geophysical Journal International, doi:10.1111/j.1365-246X.2012.05692.x

Robinson, P., Harrison, R. H., Miyajima, N., McEnroe, S.A. and Fabian, K. (2012) Chemical and magnetic properties of rapidly cooled metastable ferri-ilmenite solid solutions: II. Chemical changes during quenching and annealing. *Geophysical Journal International,* 188, 447-472.

Robinson, P., McEnroe S. A, Fabian K., Harrison, R. J., Thomas, C. I. and Mukai, H. (2014) Chemical and magnetic properties of rapidly cooled metastable ferri-ilmenite solid solutions: IV. The fine structure of self-reversed thermo-remanent magnetization, Geophysical Journal International.) doi: 10.1093/gji/ggt486.

Sadeh, B., Doi M., Shimizu, T., Matsui, M.J. (2000) Dependence of the Curie temperature on the diameter of $Fe_3O_4$ Ultra fine particles, Journal of the Magnetic Society of Japan. 24, 511–514.

Shcherbakov, V., Fabian, K., Sycheva, N., McEnroe, S. A. (2012) Size and shape dependence of the magnetic ordering temperature in nanoscale magnetic particles, Geophys. J. Int., 191, 954–964.

Schmidt, P.W., Clark, D.A. and Rajagopalan, S. (1993) An historical perspective of the Early Palaeozoic APWP of Gondwana: New results from the Early Ordovician Black Hill Norite of South Australia. Exploration Geophysics 24, 257–262.

Schmidt, P.W., McEnroe, S.A., Clark, D.A. and Robinson, P. (2007) Magnetic properties and potential field modeling of the Peculiar Knob metamorphosed iron formation, South Australia: an analog for the source of the intense Martian magnetic anomalies?  Journal of Geophysical Research, 112, B03102, doi:10.1029/2006JB004495.

Shive, P.N. and Butler, R.F. (1969) Stresses and magnetostrictive effects of lamellae in the titanomagnetite and ilmenohematite series. Journal of Geomagnetism and Geoelectricity, 21, 781- 796.

Strangway, D., Larson, E., and Goldstein, M. (1968), A possible cause of high magnetic stability in volcanic rocks, Journal of Geophyical Research-Solid Earth, 73, 3787–3795

Sauerzapf, U., Lattard, D., Burchard, M. and Engelmann R. (2008), The titanomagnetite-ilmenite equilibrium: New experimental data and thermo-oxybarometric application to the crystallization of basic to intermediate rocks, Journal of Petrology, 49, 1161–1185, doi:10.1093/petrology/egn021.

26

Wechsler, B.A. and Prewitt, C.T. (1981) Crystal structure of ilmenite (FeTiO$_3$) at high temperature and at high pressure. American Mineralogist 69, 176-185.

**Figure Captions**

**Fig. 1** Back-scatter electron (BSE) image of large trellis ilmenite oxy-exsolution lamellae on the (111) octahedral planes of magnetite. Poorly resolved later generations of exsolution are probably also ilmenite. Bright white grain is pyrite.

**Fig. 2** Ternary phase diagram of the system FeO-1/2Fe$_2$O$_3$-TiO$_2$ as used by Lindsley (1991) Properties described in text. Abbreviations: Fpb=Ferropseudobrookite; Psb=Pseudobrookite; Ilm=Ilmenite; Hem=Hematite; Usp=Ulvöspinel; Mag=Magnetite. Reactions: A) Oxy-exsolution of ilmenite from primary titanomagnetite. B) Reduction exsolution of magnetite from primary ferri-ilmenite. C) Production of magnetite by reduction in primary hematite. D) Reduction exsolution of magnetite from Ilmenite 40 solid solution (composition shift exaggerated).

**Fig. 3** BSE image of magnetite reduction-exsolution lamellae (bright) in an ilmenite host (dark) from Black Hill Norite, South Australia. The parallel sides and blunt ends of the lamellae distinguish these from hematite lamellae.

**Fig. 4** Reflected-light photomicrograph of fine lamellae, up to ~200 nm thick, parallel to (001) of hematite from Peculiar Knob, South Australia. EMP analyses and magnetic behavior indicate these are either magnetite or magnetite-maghemite solid solution (Schmidt et al. 2007). The hematite host can be distinguished from magnetite by its bireflectance, here set at its darkest orientation. Photographed with the hematite (anisotropic) at extinction and with a blue filter. As compared to Figure 3, the lamellar boundaries are very irregular, perhaps reflecting an origin for this intergrowth that was not simple reduction-exsolution.

**Fig. 5** Magnetic saturation (M$_S$), Magnetic remanence (M$_R$) and susceptibility curves for sample 246.6b from the Peculiar Knob Deposit, South Australia, determined from

quarter hysteresis loops in fields up to 1.5 T according to Fabian et al. (2013). Gray lines mark the determined $575^{\circ}$C $T_C$ of magnetite and $675^{\circ}$C $T_N$ of hematite as determined by the $1^{st}$ derivative of $M_S$ . Low-field susceptibility curve shows a peak just below $575^{\circ}$C for magnetite, and $675^{\circ}$C for the hematite, whereas the high-field susceptibility peak only shows for ferrimagnetic magnetite at $575^{\circ}$C.

**Fig. 6** Magnetic saturation ($M_S$) remanence ($M_R$) and susceptibility curves with temperature for synthetic metastable disordered titanohematite (Ilm 40) with minor reduction-exsolution lamellae of magnetite parallel to (001) of the host. Gray lines mark the $T_N$ of Ilm40 at $345^{\circ}$C and the $T_C$ of magnetite at $535^{\circ}$C. The $M_S$ increase up to ~$150^{\circ}$C may originate from interface coupling, or from insufficient saturation in 1.5 T although the latter is not discernible in the individual curves. Same method as in Fig. 5.

**Fig. 7 A)** Dark-field TEM image of synthetic Ilm 40 with exsolution lamellae of magnetite parallel to (001) of the host. Image is taken through the reflection 104 ('g: 104') of hematite and illustrates the very small proportion of magnetite. **B)** High-resolution lattice-fringe TEM image showing two lamellae of magnetite in the synthetic Ilm 40. Both are taken along a zone axis normal to $c^*_h$ (hematite) and $111^*_c$ (magnetite), and also normal to $a^*_h$ (hematite) and $-2\ 0\ 2^*_c$ (magnetite). Because the zone axis is parallel to hematite (001) (see Fig. 9), the high-resolution image indicates magnetite lamellar thicknesses of ~4.4–5.8 nm. When compared to the 1.454 nm thickness for the six layers of magnetite normal to (111), this indicates the lamellae are generally 3-4 unit cells thick with 18 up to a maximum of 24 cation layers.

**Fig. 8** TEM images of ilmenite with magnetite exsolution from the Black Hill Norite. **A)** Low- resolution bright-field image showing the ilmenite-magnetite interface accompanied by separate lattice images in common orientation of ilmenite and of

28

magnetite. Taken along a zone axis perpendicular in common to $c$* ilmenite, 111* of magnetite, $a_1$* of ilmenite and 2 0 -2*. **B)** High-resolution lattice-fringe image of magnetite-ilmenite interface resolving individual layers of magnetite parallel to (111) taken along the same zone axis as in A, and an SAED pattern (inset) from both phases and the interface.

**Fig. 9** Geometrical sketch, based on Fig. 7B, showing that -2 0 2* of magnetite is a line (violet) along the edge of a (111) octahedral plane of magnetite, that is also parallel to $a$* of hematite, where the magnetite plane (111) and the hematite plane (001) are identical in orientation. The zone axis (green line) normal to these lines is also normal to $c$* of hematite and 111* of magnetite, therefore parallel to those planes. Thus, the high-resolution image of Fig. 7B is correctly oriented to observe the magnetite lamellar thickness.

**Fig. 10** Geometrical sketch of the common plane between magnetite and hematite, showing the correspondence between -2 0 2*$_c$ (of magnetite) and $a$*$_h$ (of hematite) with generalized position of Fe octahedral in that plane. The six yellow octahedra surrounding one vacancy are those that can be in common between the two phases.

**Fig. 11** Sketches using schematic symmetrical octahedra to show possible configurations of Fe octahedra on common planes between ilmenite-hematite and magnetite. Dashed black lines are an outline of the supercell used in discussions. A) Di-octahedral array of octahedrons as in hematite and ilmenite with 8 out of 12 possible positions filled. Yellow-shaded octahedra have quasi-identical positions in both hematite and magnetite, making up 6 out of 12 possible positions. Green-shaded octahedra are those added to bring their total to 8. B) Three-quarters-octahedral array as in the octahedral layers of magnetite with 9 out of 12 possible positions filled. Yellow-shaded octahedra have quasi-identical positions in both hematite and magnetite, making up 6 out of 12 possible

positions. Green-shaded octahedra are those added to bring their total to 9. Trigonal symmetry is preserved in both 11A and 11B.    C) Array of polyhedra in the tetrahedral-octahedral layer of cubic oxides, here shaded lightly and arranged to fit on the bottom of the octahedral layers in 11A and 11B. D) The same array of polyhedra in the tetrahedral-octahedral layer of cubic oxides, here shaded heavily and arranged to fit on the top of the octahedral layers in 11A and 11B. E) Tetrahedral-octahedral layer of Figure 11C fitted on the front of the di-octahedral layer of Figure 11A. This requires face sharing between half of the upward-pointing red tetrahedra and the green underlying octahedra, a feature unknown in magnetite. F) Tetrahedral-octahedral layer of Figure 11C fitted on front of the 3/4 octahedral layer of Figure 11B. Except for minor distortions, this is the structure of magnetite. There is no face-sharing and all upward-pointing red tetrahedrons in the tetrahedral-octahedral layer fit over vacancies in the underlying octahedral layer.

**Fig. 12** Details of the structure of hematite (Blake at al. 1966) showing differently oriented trigonal symmetry features in two adjacent (001) layers. Violet dashed edges of shared octahedral faces in red upper layer correspond exactly to violet solid edges of shared octahedral faces in blue lower layer, all parallel to (001). The shared faces are consistently smaller than the unshared faces.  Illustrated are the first two layers stacked along *c* of a unit cell, where a seventh layer would be identical to the blue layer.

**Fig. 13** Details of the structure of magnetite (Fleet 1984), showing **A)** A layer of slightly distorted octahedra parallel to (111). Red octahedral edges are at angles of ~58° and ~62° from each other. Orange lines indicate hexagonal unit-cell footprint with '*a*'= 5.9369Å. **B)** A tetrahedral-octahedral layer parallel to (111) where the octahedra are symmetrical. Also shows unit-cell footprint. **C)** Fitting together of an octahedral layer above a tetrahedral layer, all with perfect three-fold symmetry. Octahedral edges with

heavier violet lines are shared between tetrahedral-octahedral and octahedral layers.
There are no shared faces. Except for slight distortions, this is identical to Figure 11F.

**Fig. 14 A**) Single (001) dioctahedral layer of ilmenite with three ilmenite unit cells outlined in
orange with 'a'= 5.08854Å. **B)** Single (111) ¾ octahedral layer of magnetite with
hexagonal unit-cell footprint outlined in orange with '***a***'= 5.9369Å and informal
ilmenite-like unit-cell footprint for magnetite outlined in green with '***a***' = 4.5702Å. **C)**
Magnetite layer overlain by ilmenite in optimal fit position with ilmenite unit-cell
footprint outlined in orange and informal ilmenite-like unit-cell footprint for magnetite
outlined in green. Corresponding ilmenite and magnetite oxygen positions are marked
in blue and red respectively. **D)** Corresponding ilmenite and magnetite oxygen positions,
emphasizing increasing strain with distance away from the initial best fit position on the
interface.

**Fig. 15** Estimated magnetic properties of a magnetite lamella in a hematite host (see text).
Six-layer repeat sequences ABCDEF of both phases are marked to show that, in this
model, contact octahedral layers are both in C positions. The contact region also
involves unusual contact tetrahedral-octahedral layers, so that the lamellar component
involves no less than five different layers.

**Fig. 16** Estimated magnetic properties of a magnetite lamella in an ilmenite host (see text).
Contact octahedral layers are both in C positions of the layer sequence. Because the
tetrahedral-octahedral layers adjacent to the contact layers are the same as in
conventional magnetite, the lamellar component only involves three different layers.

**Table 1, Part 1 Total Charge Balance**

**SIMPLE MAGNETITE**

| Layer Type | Coordination | Cation No. | Charge | Total |
|---|---|---|---|---|
| **1st 2  cat. layers** | | | | |
| Oxygen above | | 6 | -2 | -12 |
| **Magnetite Oct.** | **6** | **9** | **2.5** | **22.5** |
| Middle oxygen | | 12 | -2 | -24 |
| **Mag. Tet-Oct** | **6** | **3** | **2.5** | **7.5** |
| | **4** | **6** | **3** | **18** |
| Oxygen below | | 6 | -2 | -12 |
| Negative Charge | | | | **-48** |
| Positive Charge | | | | **48** |
| | | | | |
| **2nd 2 cat. layers** | | | | |
| Oxygen above | | 6 | -2 | -12 |
| **Mag. Tet-Oct** | **6** | **3** | **2.5** | **7.5** |
| | **4** | **6** | **3** | **18** |
| Middle oxygen | | 12 | -2 | -24 |
| **Magnetite Oct.** | **6** | **9** | **2.5** | **22.5** |
| Oxygen below | | 6 | -2 | -12 |
| Negative Charge | | | | **-48** |
| Positive Charge | | | | **48** |

**Table 1, Part 2. Total Charge B**

**HEMATITE ABOVE MAGNETITE**

| Layer Type | Coordination |
|---|---|
| **1st 2  cat. layers** | |
| Oxygen above | |
| **Hematite Oct** | **6** |
| Middle oxygen | |
| **Mag. Tet-Oct** | **6** |
| | **4** |
| (unusual)* | **4** |
| Oxygen below | |
| Negative Charge | |
| Positive Charge | |
| ChargeImbal/Ox | |
| Fract/2 = % | |
| | |
| **2nd 2 cat. layers** | |
| Oxygen above | |
| **Mag. Tet-Oct** | **6** |
| | **4** |
| (unusual)* | **4** |
| Middle oxygen | |
| **Magnetite Oct.** | **6** |
| Oxygen below | |
| Negative Charge | |
| Positive Charge | |
| ChargeImbal/Ox | |
| Fract/2 = % | |
| | |
| **3rd 2 cat. layers** | |
| Oxygen above | |
| **Magnetite Oct.** | **6** |
| Middle oxygen | |
| **Mag. Tet-Oct** | **6** |

**4**

Oxygen below
Negative Charge
Positive Charge
ChargeImbal/Ox
Fract/2 = %

\* Assignment of a nominal charg
  inverse spinel is unusual and he
  to charge balance.

## Balance

### AND CONTINUING

| Cation No. | Charge | Total |
|---|---|---|
| 6 | -2 | -12 |
| **8** | **3** | **24** |
| 12 | -2 | -24 |
| 3 | 2.5 | 7.5 |
| 4 | 3 | 12 |
| **2** | **2.5** | **5** |
| 6 | -2 | -12 |
| | | **-48** |
| | | **48.5** |
| | | 0.0104 |
| | | 0.0052 |
| | | |
| 6 | -2 | -12 |
| 3 | 2.5 | 7.5 |
| 4 | 3 | 12 |
| **2** | **2.5** | **5** |
| 12 | -2 | -24 |
| **9** | **2.5** | **22.5** |
| 6 | -2 | -12 |
| | | **-48** |
| | | **47** |
| | | -0.0208 |
| | | -0.0104 |
| | | |
| 6 | -2 | -12 |
| **9** | **2.5** | **22.5** |
| 12 | -2 | -24 |
| **3** | **2.5** | **7.5** |

## Table 1, Part 3 Total Charge Balance

### ILMENITE ABOVE MAGNETITE AND CONTINUING

| Layer Type | Coordination | Cation No. | Charge | Total |
|---|---|---|---|---|
| **1st 2  cat. layers** | | | | |
| Oxygen above | | 6 | -2 | -12 |
| **Ilmenite Fe Layer** | **6** | **8** | **2** | **16** |
| Middle oxygen | | 12 | -2 | -24 |
| **Ilmenite Ti Layer** | **6** | **8** | **4** | **32** |
| Oxygen below | | 6 | -2 | -12 |
| Negative Charge | | | | **-48** |
| Positive Charge | | | | **48** |
| ChargeImbal/Ox | | | | 0.0000 |
| Fract/2 = % | | | | 0.0000 |
| | | | | |
| **2nd 2 cat. layers** | | | | |
| Oxygen above | | 6 | -2 | -12 |
| **Ilmenite Ti Layer** | **6** | **8** | **4** | **32** |
| Middle oxygen | | 12 | -2 | -24 |
| **Ilmenite Contact** | **6** | **5** | **2** | **10** |
| **(unusual)\*\*** | **6** | **3** | **3** | **9** |
| Oxygen below | | 6 | -2 | -12 |
| Negative Charge | | | | **-48** |
| Positive Charge | | | | **51** |
| ChargeImbal/Ox | | | | 0.0625 |
| Fract/2 = % | | | | 0.0313 |
| | | | | |
| **3rd 2 cat. layers** | | | | |
| Oxygen above | | 6 | -2 | -12 |
| **Ilmenite Contact** | **6** | **5** | **2** | **10** |
| **(unusual)\*\*** | **6** | **3** | **3** | **9** |
| Middle oxygen | | 12 | -2 | -24 |
| **Mag. Tet-Oct** | **6** | **3** | **2.5** | **7.5** |
| | **4** | **6** | **3** | **18** |
| Oxygen below | | 6 | -2 | -12 |

| | | |
|---|---|---|
| **6** | **3** | **18** |
| 6 | -2 | -12 |
| | | **-48** |
| | | **48** |
| | | 0.0000 |
| | | 0.0000 |

e of +2.5 to a tetrahedral site of an
re only used ad hoc to come close to

| Negative Charge | | | **-48** |
|---|---|---|---|
| Positive Charge | | | **44.5** |
| ChargeImbal/Ox | | | -0.0729 |
| Fract/2 = % | | | -0.0365 |

**4th 2 cat. layers**

| | | | | |
|---|---|---|---|---|
| Oxygen above | | 6 | -2 | -12 |
| **Mag. Tet-Oct** | **6** | **3** | **2.5** | **7.5** |
| | **4** | **6** | **3** | **18** |
| Middle oxygen | | 12 | -2 | -24 |
| **Magnetite Oct** | **6** | **9** | **2.5** | **22.5** |
| Oxygen below | | 6 | -2 | -12 |
| Negative Charge | | | | **-48** |
| Positive Charge | | | | **48** |
| ChargeImbal/Ox | | | | 0.0000 |
| Fract/2 = % | | | | 0.0000 |

** Assignment of a charge of +3 to positions in an octahedral contact layer against an ilmenite Ti layer above and a magnetite tetra-hedral - octahedral layer below was done ad hoc to come closer to charge balance.

**Table 1, Part 4 Total Charge Balance**

**ILMENITE ABOVE AGAINST HEMATITE BELOW**

| Layer Type | Coordination | Cation No. | Charge | Total |
|---|---|---|---|---|
| **1st 2 cat. layers** | | | | |
| Oxygen above | | 6 | -2 | -12 |
| **Ilmenite Fe Layer** | **6** | **8** | **2** | **16** |
| Middle oxygen | | 12 | -2 | -24 |
| **Ilmenite Ti Layer** | **6** | **8** | **4** | **32** |
| Oxygen below | | 6 | -2 | -12 |
| Negative Charge | | | | **-48** |
| Positive Charge | | | | **48** |
| ChargeImbal/Ox | | | | 0.0000 |
| Fract/2 = % | | | | 0.0000 |
| | | | | |
| **2nd 2 cat. layers** | | | | |
| Oxygen above | | 6 | -2 | -12 |
| **Ilmenite Ti Layer** | **6** | **8** | **4** | **32** |
| Middle oxygen | | 12 | -2 | -24 |
| **Contact Layer** | **6** | **4** | **2** | **8** |
| **\*\*\*** | **6** | **4** | **3** | **12** |
| Oxygen below | | 6 | -2 | -12 |
| Negative Charge | | | | **-48** |
| Positive Charge | | | | **52** |
| ChargeImbal/Ox | | | | 0.0833 |
| Fract/2 = % | | | | 0.0417 |
| | | | | |
| **3rd 2 cat. layers** | | | | |
| Oxygen above | | 6 | -2 | -12 |
| **Contact Layer** | **6** | **4** | **2** | **8** |
| **\*\*\*** | **6** | **4** | **3** | **12** |
| Middle oxygen | | 12 | -2 | -24 |
| **Hematite Fe Layer** | **6** | **8** | **3** | **24** |
| Oxygen below | | 6 | -2 | -12 |
| Negative Charge | | | | **-48** |

| | | | | |
|---|---|---|---|---|
| Positive Charge | | | | **44** |
| ChargeImbal/Ox | | | | -0.0833 |
| Fract/2 = % | | | | -0.0417 |
| | | | | |
| **4th 2 cat. layers** | | | | |
| Oxygen above | | 6 | -2 | -12 |
| **Hematite Fe Laye** | **6** | **8** | **3** | **24** |
| Middle oxygen | | 12 | -2 | -24 |
| **Hematite FeLayer** | **6** | **8** | **3** | **24** |
| Oxygen below | | 6 | -2 | -12 |
| Negative Charge | | | | **-48** |
| Positive Charge | | | | **48** |
| ChargeImbal/Ox | | | | 0.0000 |
| Fract/2 = % | | | | 0.0000 |

*** The mixed valence contact layer is a standard feature of attributed
    to lamellar magnetism (see Robinson et al. 2006a).
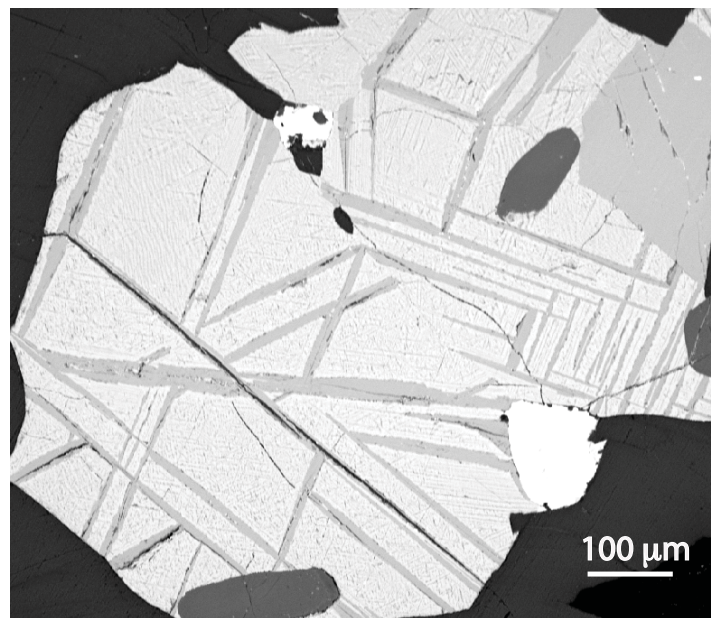
Fig. 1
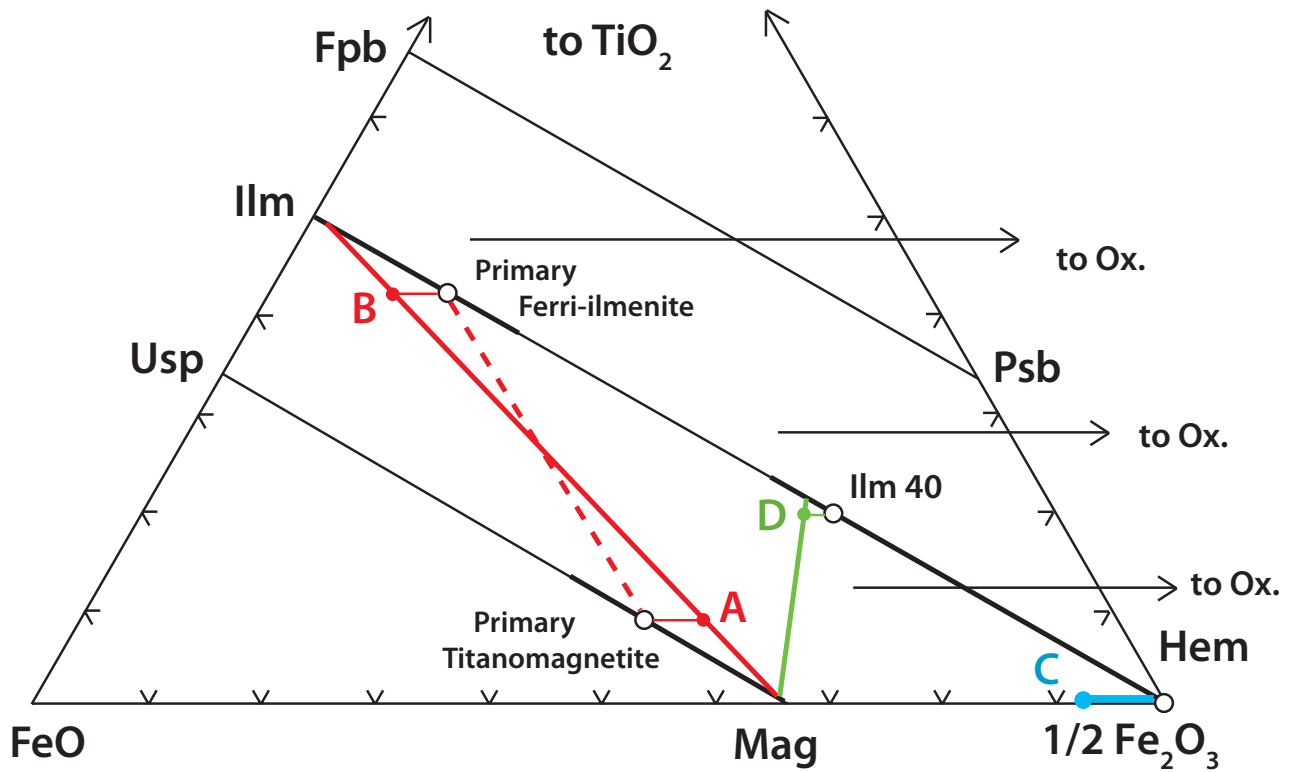
Fig. 2
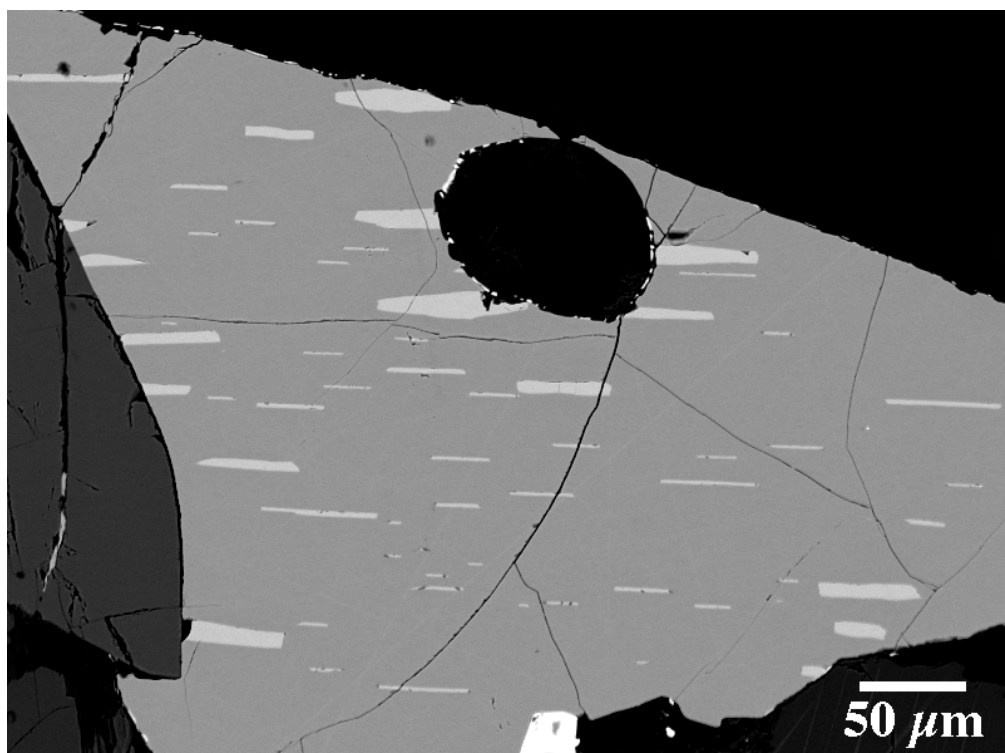
Fig. 3
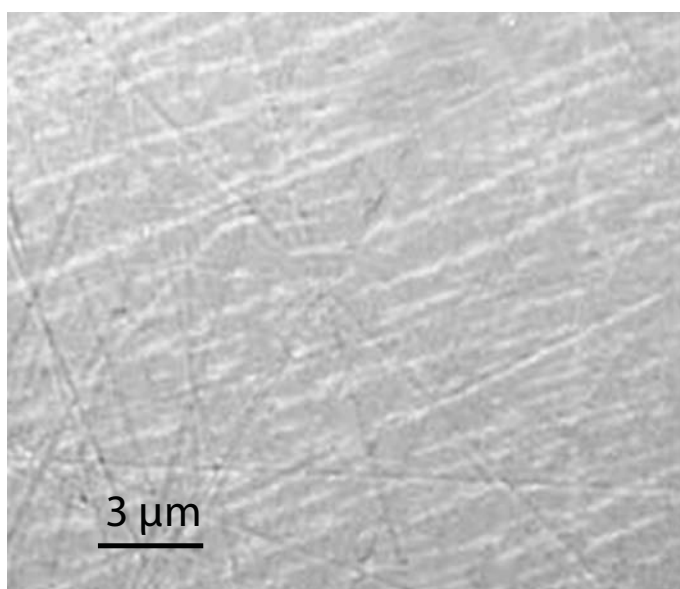
Fig. 4

Fig. 5

Fig. 6

Fig. 7

Fig. 8

Fig. 9

Octahedral edge parallel to (010)c

Octahedral edge parallel to (100)c
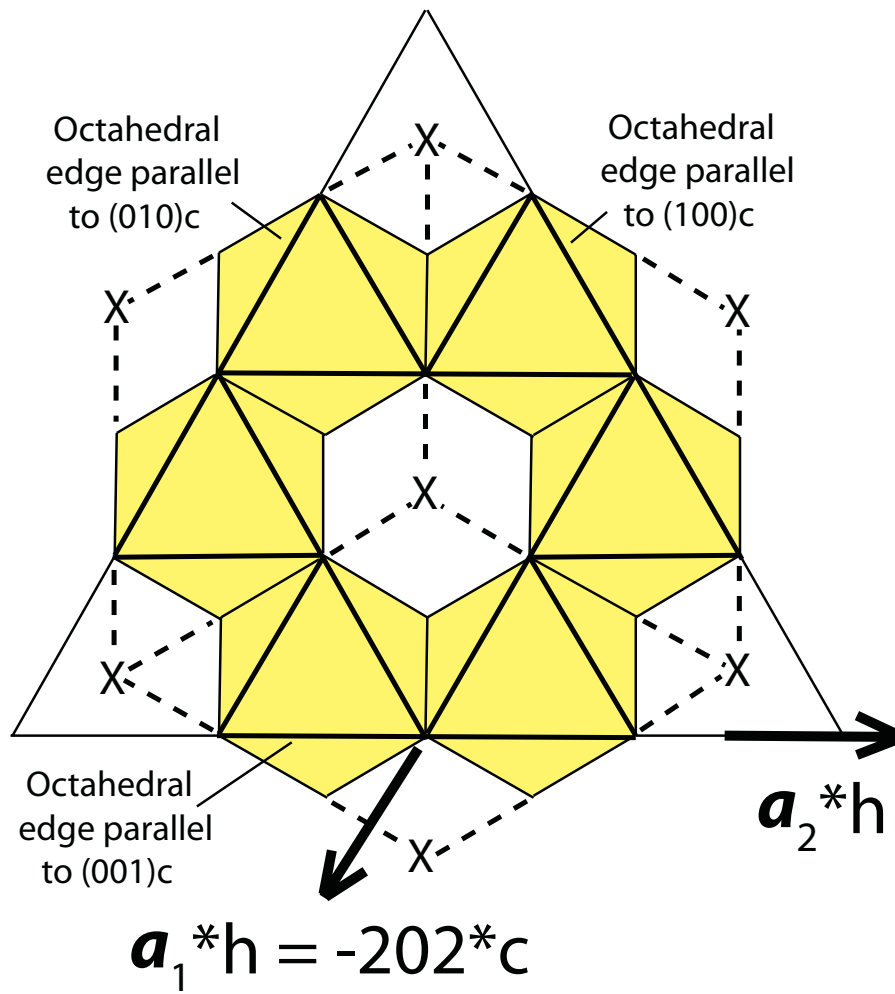
Octahedral edge parallel to (001)c
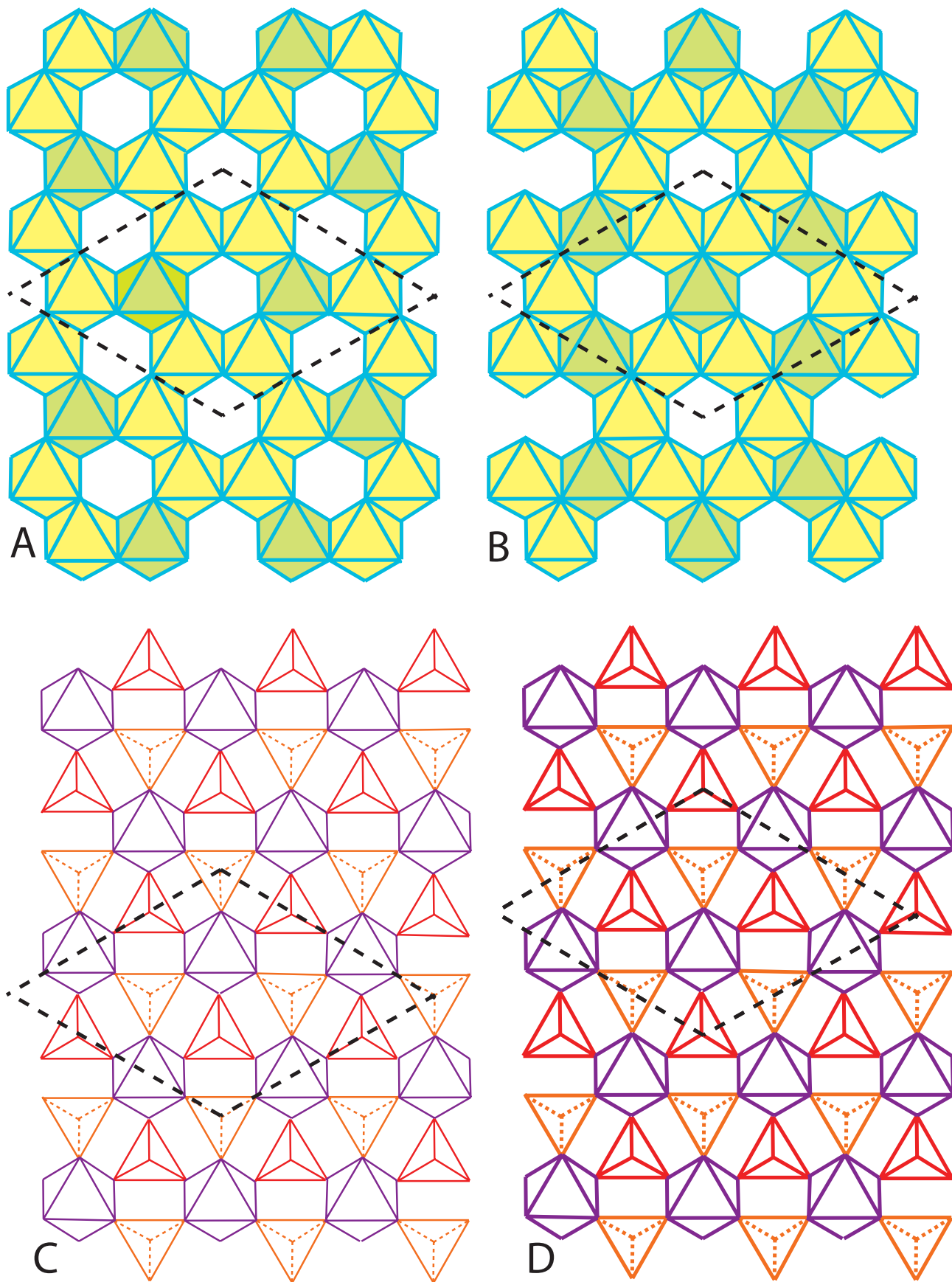
$\boldsymbol{a}_2*h$
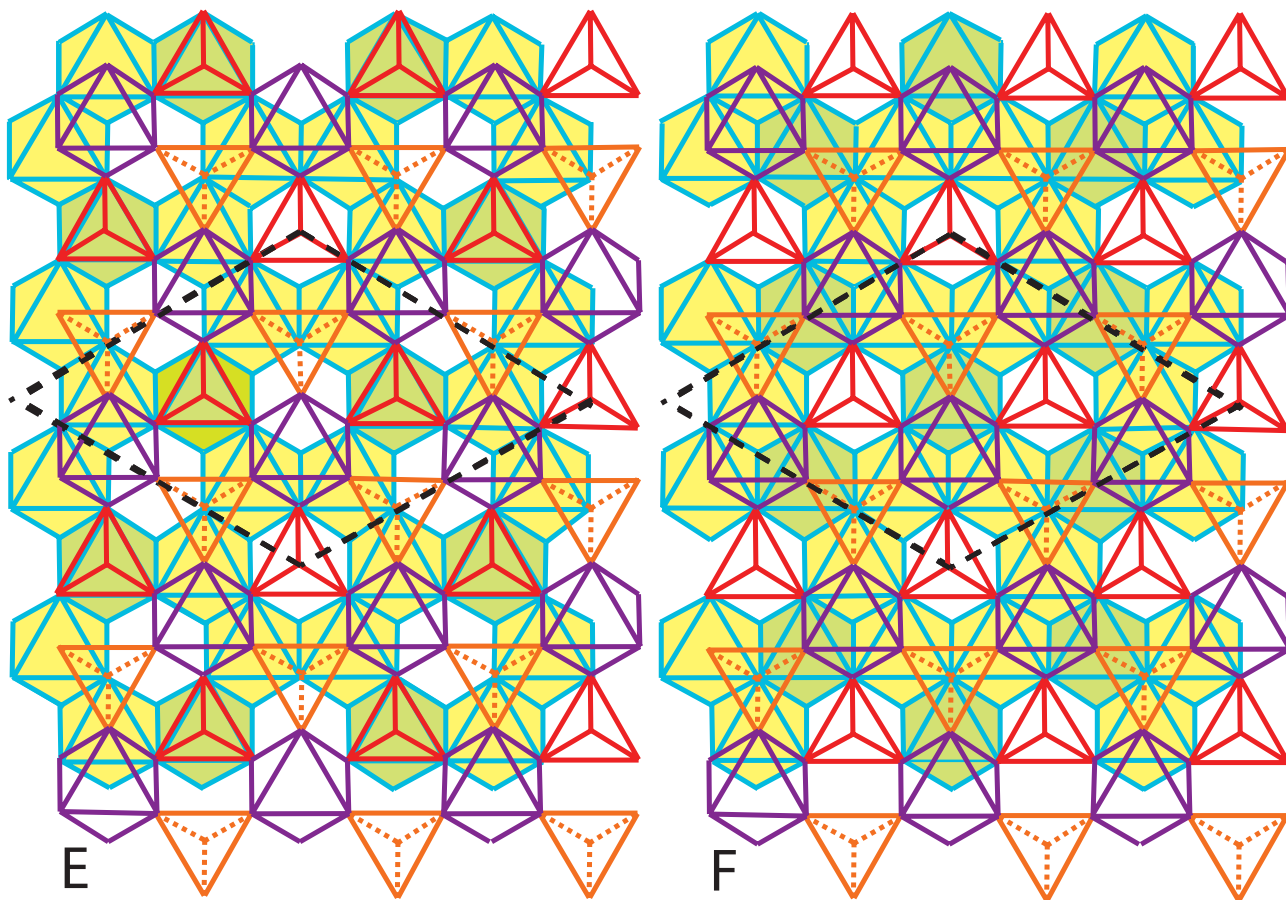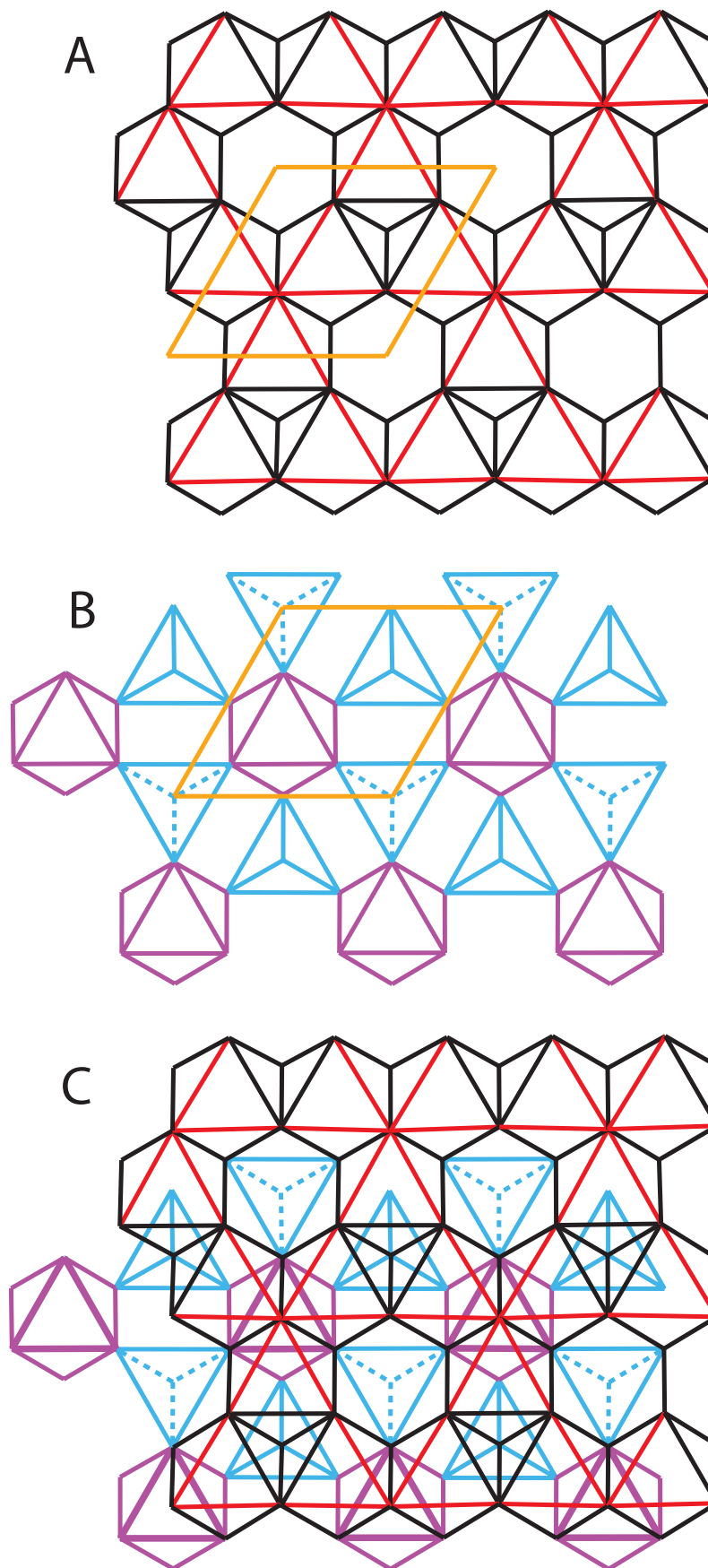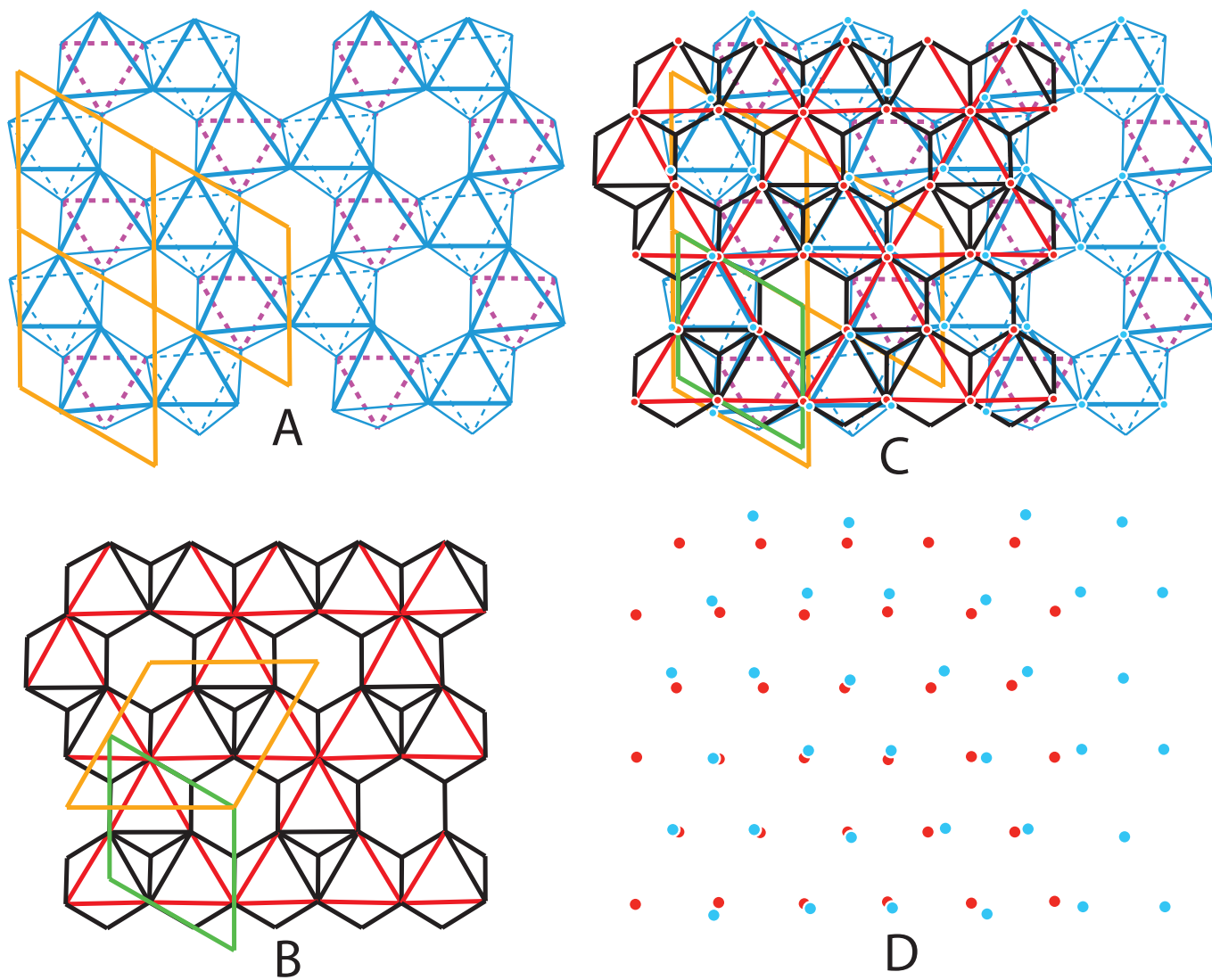
$\boldsymbol{a}_1*h = -202*c$
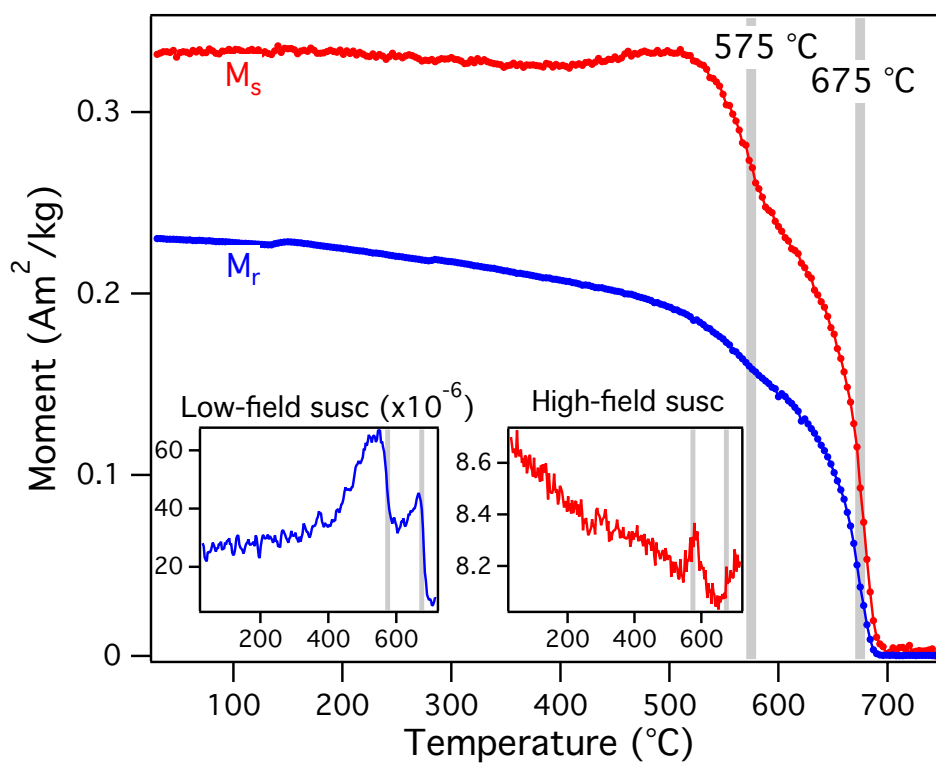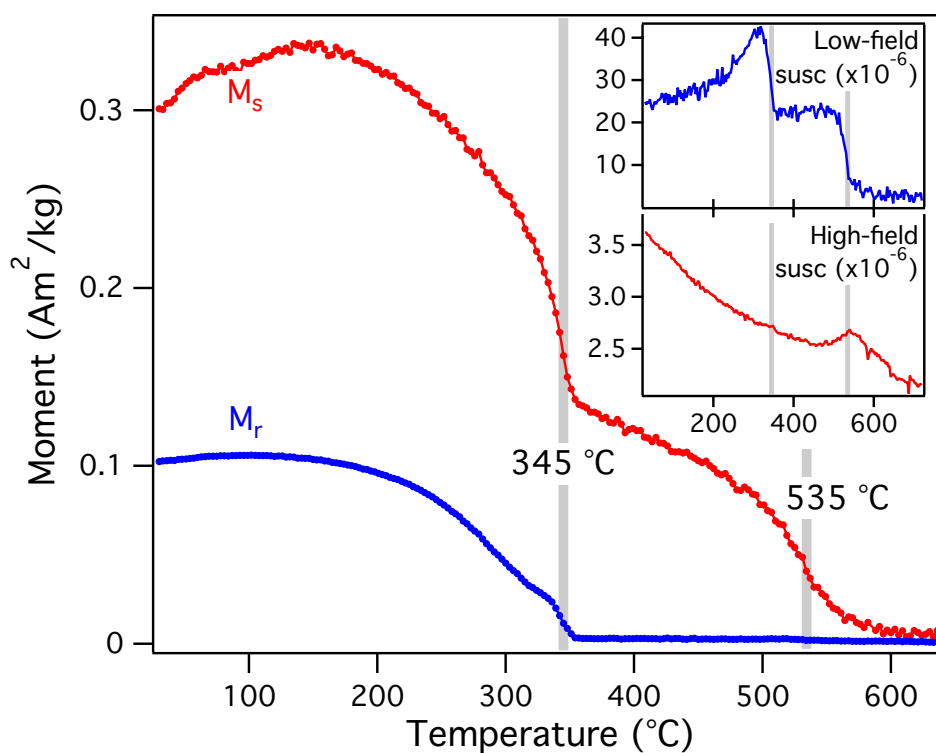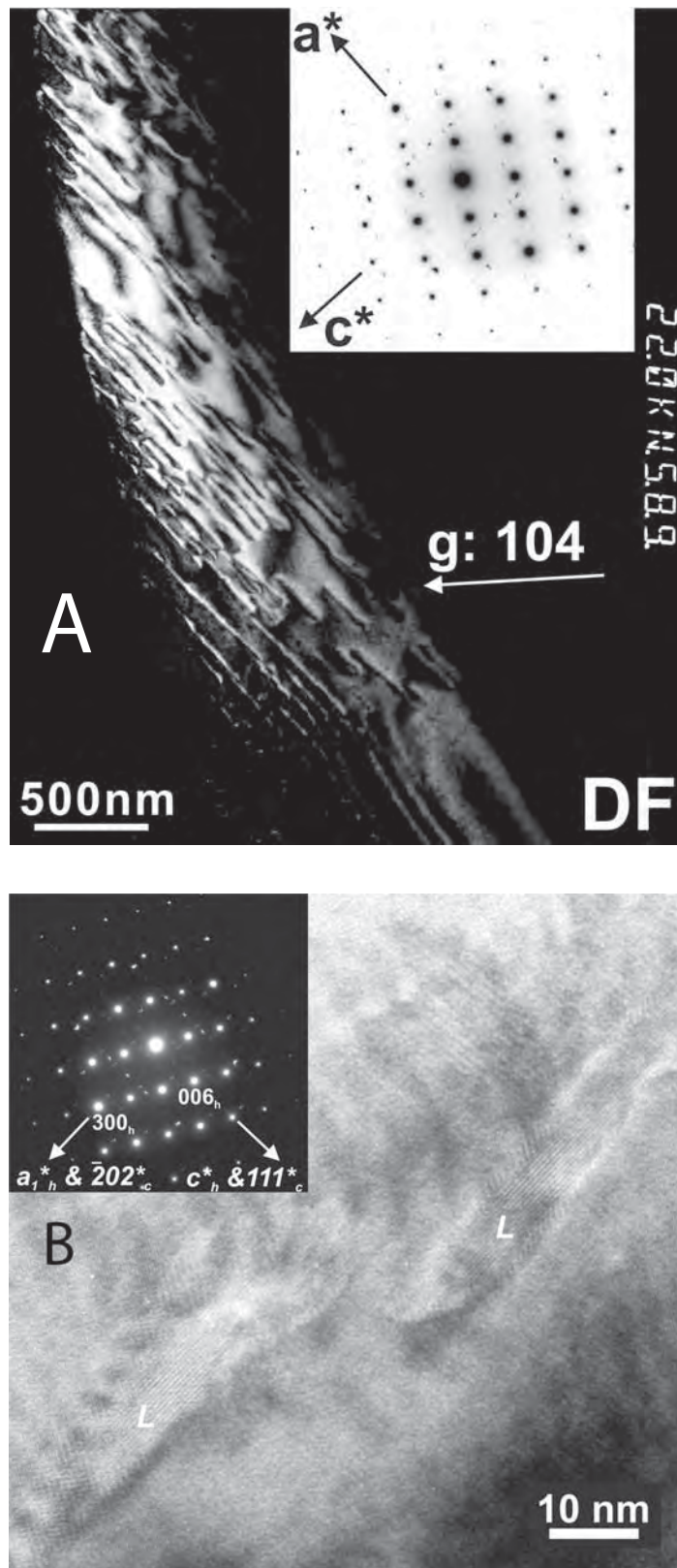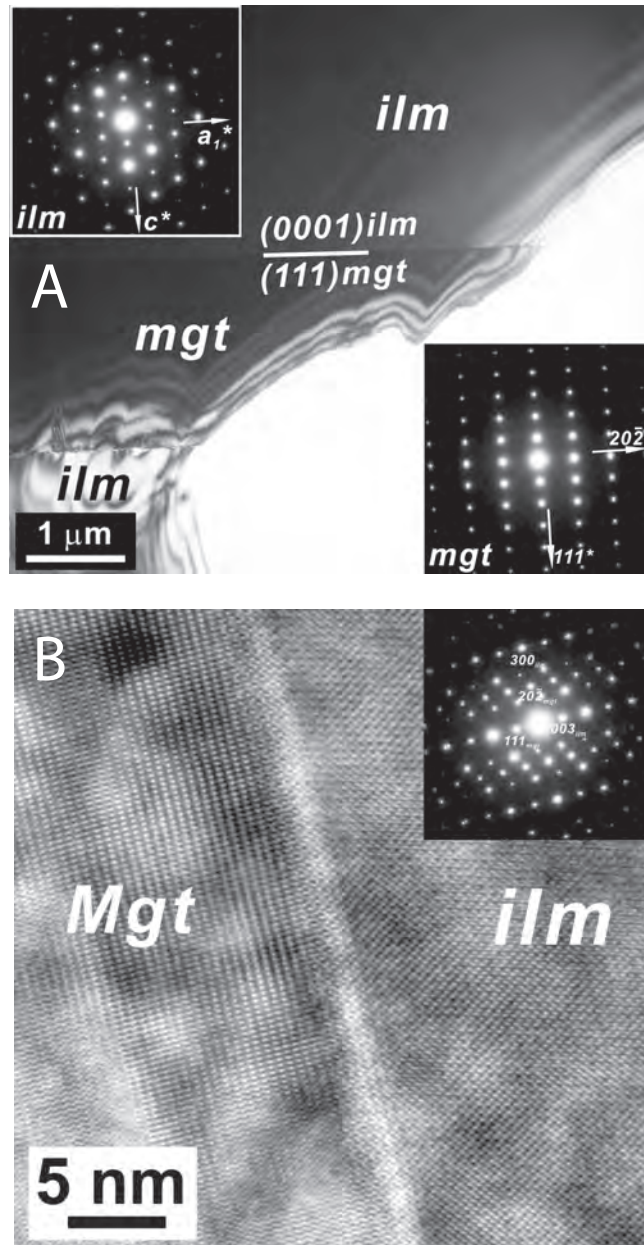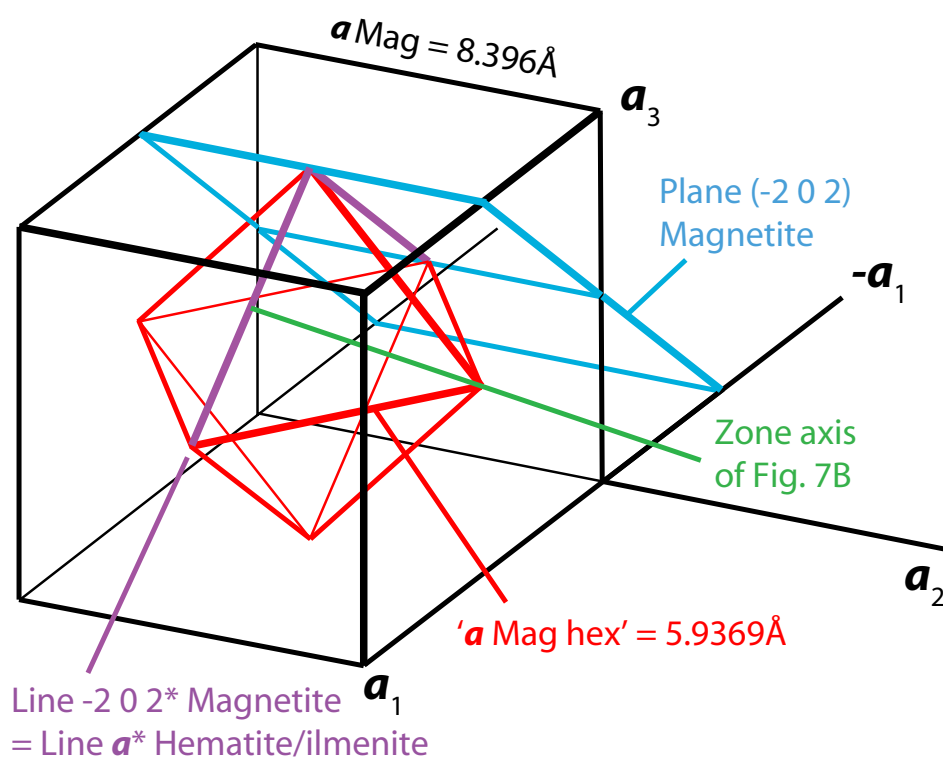
Fig. 10

Fig. 11

Fig. 11 E,F
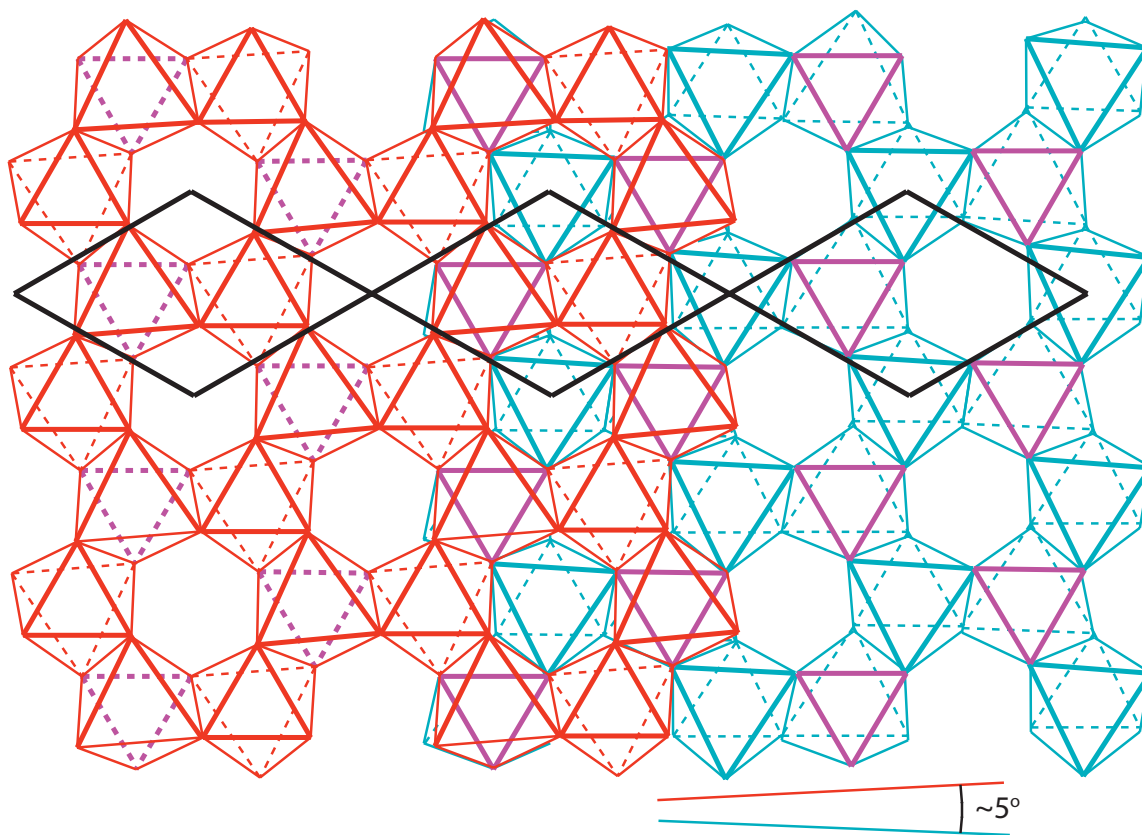
Fig. 12

Fig. 13

Fig. 14

## Magnetite Lamella in Hematite Host

| | | | | |
|---|---|---|---|---|
| 1A | HEM OCT | $8\ Fe^{3+}$ | → | $+40\ \mu B$ |
| 2B | HEM OCT | $8\ Fe^{3+}$ | ← | $-40\ \mu B$ |
| 3C | CONTACT | $8\ Fe^{3+}$ | → | $+40\ \mu B$ |
| 4D | MAG TET-OCT | $3Fe^{2.5+}-4Fe^{3+}-2Fe^{2.5+}$ | ← | $+13.5-29=-15.5\mu B$ |
| 5E | MAG OCT | $9\ Fe^{2.5+}$ | → | $+40.5\ \mu B$ |
| 6F | MAG TET-OCT | $3\ Fe^{2.5+}-6\ Fe^{3+}$ | ← | $+13.5-30=-16.5\mu B$ |
| 7A | MAG OCT | $9\ Fe^{2.5+}$ | → | $+40.5\ \mu B$ |
| 8B | MAG TET-OCT | $3Fe^{2.5+}-4Fe^{3+}-2Fe^{2.5+}$ | ← | $+13.5-29=-15.5\mu B$ |
| 9C | CONTACT | $8\ Fe^{3+}$ | → | $+40\ \mu B$ |
| 10D | HEM OCT | $8\ Fe^{3+}$ | ← | $-40\ \mu B$ |
| 11E | HEM OCT | $8\ Fe^{3+}$ | → | $+40\ \mu B$ |
| 12F | HEM OCT | $8\ Fe^{3+}$ | ← | $-40\ \mu B$ |

**Lamellar Part**
80-71= 9 µB

**Magnetite Part**
94.5-30 = 64.5 µB

Total     $+73.5\ \mu B$

## Fig. 15

## Magnetite Lamella in Ilmenite Host

| | | | | |
|---|---|---|---|---|
| 1A | ILM OCT | $8\ Fe^{2+}$ | | $0\ \mu B$ |
| 2B | ILM OCT | $8\ Ti^{4+}$ | | $0\ \mu B$ |
| 3C | CONTACT | $2\ Fe^{3+}+5\ Fe^{2+}$ | → | $+35\ \mu B$ |
| 4D | MAG TET-OCT | $3\ Fe^{2.5+}-6\ Fe^{3+}$ | ← | $+13.5-30=-16.5\mu B$ |
| 5E | MAG OCT | $9\ Fe^{2.5+}$ | → | $+40.5\ \mu B$ |
| 6F | MAG TET-OCT | $3\ Fe^{2.5+}-6\ Fe^{3+}$ | ← | $+13.5-30=-16.5\mu B$ |
| 7A | MAG OCT | $9\ Fe^{2.5+}$ | → | $+40.5\ \mu B$ |
| 8B | MAG TET-OCT | $3\ Fe^{2.5+}-6\ Fe^{3+}$ | ← | $+13.5-30=-16.5\mu B$ |
| 9C | CONTACT | $2\ Fe^{3+}+5\ Fe^{2+}$ | → | $+35\ \mu B$ |
| 10D | ILM OCT | $8\ Ti^{4+}$ | | $0\ \mu B$ |
| 11E | ILM OCT | $8\ Fe^{2+}$ | | $0\ \mu B$ |
| 12F | ILM OCT | $8\ Ti^{4+}$ | | $0\ \mu B$ |

**Lamellar Part**
70-16.5= 53.5µB

**Magnetite Part**
81-33 = 48µB

Total     $+101.5\mu B$

## Fig. 16